Rheinisch-Westfälische Technische Hochschule Aachen
FACULTY OF MECHANICAL ENGINEERING

Thesis

Finite Element Analysis of Gyroid and Voronoi architectures of Porous 3D-Printed Ti-6Al-4V bone replacement materials

Presented by:	Noel Jacob Ureña Sandí, Lic. B.Sc.
Study programme:	CAME
Matriculation number:	40 45 98
Reviewer:	Univ.-Prof. Dr.-Ing. Mikhail Itskov
Supervisor:	Rajesh Chandrasekaran, M.Sc.
External supervisor:	Dr.-Ing Teodolito Guillén Girón
External supervisor:	Miguel Araya Calvo, M.Sc.

Aachen, 28th of November 2022

CONTENTS

LIST OF ABBREVIATIONS

AM	Additive Manufacturing
BCC	Body-Centered Cubic
FEA	Finite Element Analysis
LVT	Laguerre-Voronoi Tesselation
PBC	Periodic Boundary Condition
RVE	Representative Volume Element
RWTH	Rheinisch-Westfälische Technische Hochschule
SLM	Selective Laser Melting
TPMS	Triply Periodic Minimal Surface

LIST OF SYMBOLS

$\boldsymbol{\sigma}$	Cauchy's Stress Tensor
$solid.RFz$	COMSOL Multiphysics z-direction Reaction Force Variable
ν	Poisson's ratio in x-direction
Φ	Porosity or Void Volume Fraction
ρ_{rel}	Relative Density
σ_e	Equivalent Stress
σ_{Eng}	Engineering Stress
σ_{Mises}	von Mises Equivalent Stress
σ_{ys0}	Initial Yield Stress
σ_{ys}	Yield Stress
ε	Uniaxial Engineering Strain
ε_{pe}	Effective Plastic Strain
E_t	Isotropic Tangent Modulus
E_{11}	Young's Modulus in x-direction
F_y	Yield function
F_z	Reaction Force in the z-direction
$F_{y\ Mises}$	von Mises Yield criterion
J_2	Second Deviatoric Stress Invariant
Q_p	Plastic Potential
$\dot{\boldsymbol{\varepsilon}}_p$	Increment of the Plastic Strain Tensor
$\dot{\boldsymbol{\varepsilon}}_{pvol}$	Volumetric Plastic Strain Rate

LIST OF FIGURES

1. ABSTRACT

Titanium and titanium-based alloys are widely used as implants for bone replacement. However, the higher Young's modulus of monolithic implants compared to the human bone's causes a weakening of the surrounding bones, ultimately causing considerably high percentages of implant rejection. Porous materials reduce the Young's modulus making it more comparable to the bones'. Finite Element simulations in COMSOL Multiphysics were used to perform simulations on Triply Periodic Minimal Surface (TPMS) gyroid, and stochastical Voronoi models generated in nTopology design software and compared with the compression results of Selective Laser Melting (SLM) manufactured compression samples. The simulations of unit cells accurately predicted the yield strength of the periodic gyroid materials for relative densities between 0.1 and 0.5, primarily when the porous plasticity Gurson model with void volume fraction between 0.05 and 0.1 was used. The prediction of the Young's modulus showed an increasing divergence from the experiments with increasing relative densities. However, an empirical rule which also worked for the Voronoi family was developed to correct this divergence. Increasing the models' size for the non-periodic Voronoi architectures proved to improve the accuracy of the yield strength prediction. The 0.5 relative density cube of 1.8 mm was large enough to be considered a Representative Volume Element (RVE) for this structure.

2. INTRODUCTION

2.1. MOTIVATION

Stress-shielding is a bone density reduction caused by a difference between the elastic modulus of bone and bone implants in segmental bone defect repair. This process induces a stress redistribution near the implant, which can cause implant loosening [57][23].

Additive Manufacturing (AM) techniques such as Selective Laser Melting (SLM) enable the production of porous architectures by using metallic materials such as titanium alloys. These porous structures have exemplary configurations for load-bearing, bone growth, reduced weight, and minimization of stress-shielding by reducing the implant's Young's modulus, making it more similar to the bone's [27].

Finite Element Analysis (FEA) contributes to the cost-effective evaluation of new porous architectures for bone replacement materials. Its main limitation is the computational expense. Microstructured materials in which the discontinuities are in the micro-scale imply a considerable computational effort to model objects of macroscopical size. Microscopic finite elements must be used to mesh the micro or meso-discontinuities. Therefore, an object of macroscopical dimensions requires many finite elements, which causes significant computation times and, in several cases, convergence issues. Different techniques have been developed to overcome this issue.

One such technique is homogenization, which was initially developed for composite materials but is also employed with porous materials [7]. Homogenization aims to treat the macrostructure as a continuous material without consideration of its microstructure, therefore reducing computing time [15].

In the case of direct computational homogenization, it is necessary to define

an RVE, the smallest material volume of a composite or porous material that can still represent the macroscopical behavior of the material. Therefore, the average mechanical properties of the RVE and the porous material's average properties are deemed equal.

Periodic Boundary Conditions (PBC) must be created for the RVE so that the porous material deformation is the same as the deformation of the RVE and separation or overlap between neighboring RVEs is avoided.

For meso and macro-structured materials, using an RVE homogenization might not be required, i.e., one can perform the FEA simulation directly on the porous material part, as long as the average size of the pores of the structure is not too small relative to the size of the part. Many authors take advantage of this by simulating small pieces of the porous material to obtain the material's stress-strain behavior. For more significant sizes, using a homogenized material model is generally less computationally expensive because only the external geometry of the part has to be modeled. The part is modeled as continuous internally, and the homogenized material model accounts for its mechanical behavior.

Periodic materials are those where a microscopical unit cell is repeated several times until the macroscopical material is generated. For periodic materials, the RVE size can be selected to have the exact size of the repeating unit cell [56],[50], [3]. However, in some cases, especially when homogenization is not performed, several unit cells of periodic materials must be assembled and simulated together for their mechanical properties to match the ones of the macroscopical material [40], [38], [68].

Stochastic architectures, as opposed to periodic ones, also exist. In stochastically architected materials, no unit cell repeats to form the macroscopic material. Instead, a randomly generated set of points is used to create the material's structure for the entire macroscopic part. Voronoi-tessellation-generated materials are one example of this type of architecture. For stochastic architectures, the size of the RVE, which still represents the macroscopical material behavior, must be determined. As the porosity of the material increases, larger RVEs are needed to obtain representative macroscopic responses [43].

On the other side, the elastic modulus is one of the most critical parameters of interest when modeling the behavior of bone replacement materials. Therefore, one could think that only the elastic regime of the dense material's stress-strain relation is of interest. However, since the porous material has thin-walled structures, internal yield occurs before the macroscopical material shows a deviation from linear elasticity. That is why an elastoplasticity model is commonly used as the constitutive model for dense material [35]. Bilinear Isotropic Hardening Models are the most commonly used, but plenty of hardening models can be tried

to determine which one resembles better the non-linear behavior of the porous material stress-strain relation.

In addition to the computational expense, simulation accuracy is another important aspect. For the simulation, the material is considered perfectly homogeneous. Instead, the parts manufactured by SLM could have a different surface roughness and topography than the idealized CAD model, as well as internal pores of unmelted powdered material [60], which cause the simulations to have higher Young's modulus and yield strength than the experimental results.

As the relative density increases, the effects introduced by the manufacturing process become more prominent as more material is sintered, which causes an additional shift between the simulation and experimental results [76], [73]. The comparison between the mechanical tests and the initial simulations allows for updating the modulus of the dense material for it to match the experimental results. This corrected modulus can be used for subsequent simulations.

The selection of the best plasticity models and parameters, the correction of the elastic modulus, and the investigation of the optimal RVE size to fit the experimental results of mechanical tests is crucial for further simulations, computational homogenization, topology optimization of these architectures and the evaluation of new ones and, finally for the implementation of user-defined material models that can be used to simulate the behavior of macroscopical bone replacement implants.

2.2. State of the Art

2.2.1. AM of Titanium bone replacement materials

Titanium alloys and pure titanium monolithic parts are widely used for orthopedic implants for bone replacement due to their excellent biocompatibility, corrosion and fatigue resistance, high strength-to-weight ratio, good ductility, excellent wear resistance, low cytotoxicity, and little tendency to provoke allergic reactions [47]. However, the high difference between the modulus of the titanium implant and the surrounding bone causes a bone density reduction known as stress shielding. This bone density reduction may cause implant failure [54]. According to [51], the stiffness of titanium, when fabricated as a porous material, decreases with the square of relative density, becoming more similar to the bone and thus decreasing stress shielding [31],[36]. The open porosity also allows complete bone ingrowth, which improves implant success and long-term survival. These advantages of porous titanium make them ideal for bone replacement implants and the subject of a substantial research effort.

Until the development of additive manufacturing methods, the manufacturing

of open porous titanium alloys was limited to pores induced by pressurized gas bubbles, superplastic expansion, space-holder technique, or partial sintering of starting powders [71]. New ways to produce porous titanium materials have been recently developed, for example, friction stir welding of titanium and zinc plates, followed by dezincification by immersion of the jointed samples in a hydrochloric acid solution, used by [66] to create an open and interconnected porous material. They all provide limited control over the pore geometry and the architecture of the material.

Additive manufacturing, on the other side, allows for greater control over the architecture. This control over the exact geometry of the material's structure allows for the design and optimization of novel architectures. Many studies have been performed evaluating different geometries. Starting from the most straightforward structures and very low porosities of around 20% [9], but quickly moving towards more complex structures and higher porosities. Different AM techniques have been used to produce titanium additively manufactured bone replacement materials: electron beam melting, SLM, and even direct ink writing [22].

[68] analyzed tetrahedron-based cell, tetrahedron cell, body-centered cubic (BCC), and octet truss cell structures and found that the strut diversities in Scanning Electron Microscope micrograph measurements indicated that the selective laser melting printing of Ti-6Al-4V scaffolds could reach high printing accuracy.

Biomaterials based on minimal surfaces showed a favorable but rare combination of relatively low elastic modulus (in the range of those observed for trabecular bone) and high yield strengths exceeding those reported for cortical bone [10]. The ratio of elastic modulus anisotropy in orthogonal directions was comparable to those of trabecular bone [4]. This architecture avoids stress shielding while providing ample mechanical support for bone tissue regeneration and osseointegration [36].

BCC and face-centered-cubic-structured plate lattice scaffolds with superior mechanical performance are proposed [69]. Their Young's modulus and yield strength are comparable with human bones and other scaffolds. In addition, relatively high permeabilities are also achieved in such scaffolds. Similar structures were fabricated [19] to examine their mechanical properties under compression, torsional loads, and different load directions. When the load acted vertically, cubic structures showed strength and stiffness values higher than the BCC and cross structures.

2.2.2. Gyroid and Voronoi architectures modeling

A minimal surface is a surface that locally minimizes its area, i.e., the total surface area is minimized subject to some constraint [7]. Triply periodic continuous minimal surfaces (TPMS) are surfaces represented by functions of form $F(x; y; z) = const.$

The gyroid triply periodic minimal surfaces is the surface generated by the following equation:

$$F\ (x; y; z)\ =\ \sin y \cos z\ +\ \sin z \cos x\ +\ \sin x \cos y\ =\ 0 \qquad (2.1)$$

Figure 2.1 shows a material generated from the volumetric repetition of a unit cell of a gyroid TPMS. The theoretical gyroid surface is given a wall thickness for fabrication purposes, which in this study will be changed to achieve different relative densities.
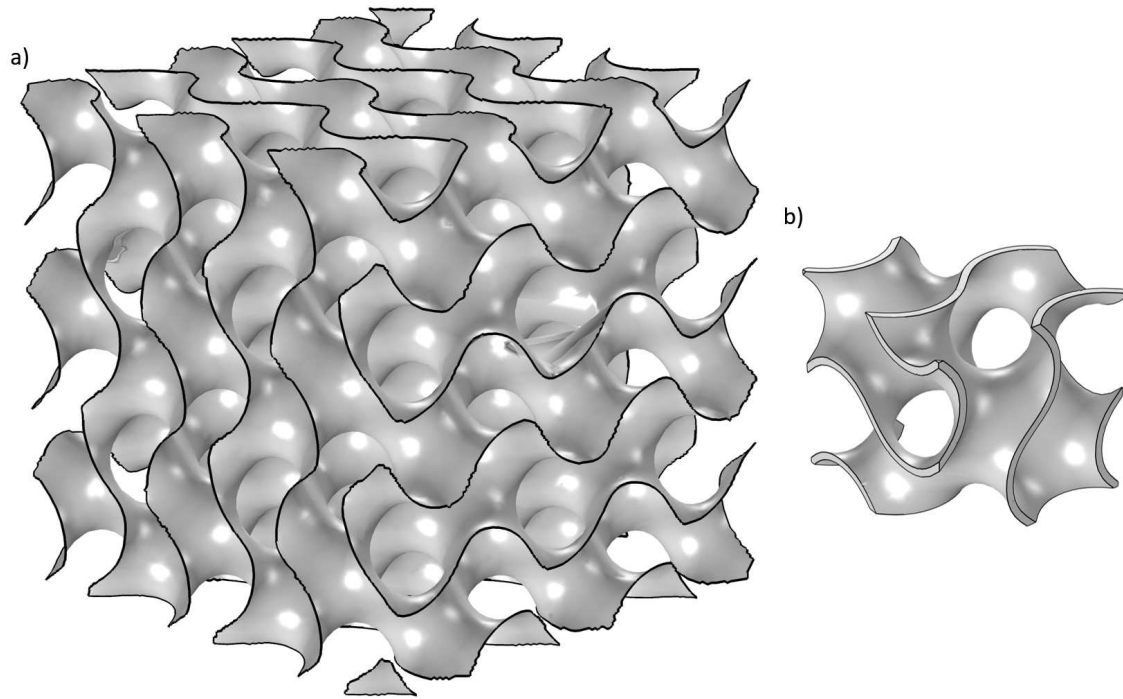

Figure 2.1.: a) Gyroid TPMS material generated from the b) gyroid unit cell.

TPMS scaffolds have attracted significant attention in bone regenerative medicine thanks to their excellent biomimetic and mechanical properties [20]. The elastic modulus and permeability of gyroid TPMS bone scaffolds of 316 L stainless steel

were found to be in the range of human bones [38]. They also showed that manufacturing accuracy increased with greater designed porosity, while the in vitro experiments revealed that permeability played the leading role in cell proliferation.

Visual and quantifiable comparisons by superimposing 3D μ-CT reconstructed models of the Ti-6Al-4V TPMS lattices on their 3D-CAD models showed excellent reproduction of the designs [72]. With existing powder bed fusion technologies, the strut and wall thicknesses range from 200 to 1669 μm [39].

On the other hand, a Voronoi tesselation is a domain subdivision into a number of distinct regions based on the same number of corresponding points, called seeds. Each region generated by this method is referred to as a Voronoi cell. Voronoi comes from the last name of the developer of this technique [67], in which polygonal shapes are formed by creating equidistant lines between any neighboring points from the randomly generated seed. Structures generated by this method are widely used to create models of many materials. [48] uses Voronoi tesselation to describe the heterogeneous morphology of biopolymer aerogels, finding that the fiber diameter, the pore-size distribution, and the density of the cells within the aerogel network show a significant influence on their mechanical response. Figure 2.1 shows an example of a Voronoi architecture RVE of 0.1 relative density and one compression sample of this same relative density.

Using Laguerre-Voronoi Tesselation (LVT) [13] shows the macroscopic stress-strain curve of bulk porous κ-carrageenan aerogels material is predicted from the pore-size distributions, solid fractions, and Young's modulus of the pore-wall fibers. LVT is a weighted version of the Voronoi tessellation where each point is assigned a weight. The position of the cell boundaries is determined by the relative value of the weights of two neighboring seeds. In LVT each Voronoi cell is generated based on a sphere. The cell boundaries can be generated as a tangent to the sphere surface at the point of contact between two adjacent spheres of different sizes rather than equidistance positioning.

Voronoi structures have also been employed to design bone implants and scaffolds for AM [28], finding an excellent potential for Voronoi tessellation to design patient-specific bone scaffolds with macro pore sizes that mimic trabecular bone geometry. However, matching feature thickness to trabecular bone thickness is not recommended for matching the mechanical properties of titanium lattice structures to those of human trabecular bone. Control of pore size, porosity, and lattice type may yield better results when replacing the trabecular bone with additively manufactured titanium lattices [39].

2.2.3. FEA of 3D-printed gyroid and Voronoi porous architectures

Simulations of porous 3D-printed titanium bone replacement materials are typically performed in parallel with experimental mechanical tests. Some authors (e.g., [73], [56], and [3] perform FEA simulations without RVEs, i.e., they simulate the actual mechanical test sample size. On the other side, [76], [65], [43], and [40] use RVEs, and even though they do not utilize PBCs nor perform computational homogenization, they can obtain relevant information from the RVEs simulations. Finally,[57] uses RVEs and PBC to obtain a homogenized material model.

[40] considers the influence of the RVE size on the ability of the simulations to predict Young's modulus and yield strength for cubic, diamond, and body-centered architectures.

FEA simulations predicted the mechanical properties of 316 L stainless steel gyroid scaffolds fabricated by Selective Laser Melting [38]. The material properties were used as reported by the powder manufacturer. Regarding the simulation, they used a model consisting of 2x2x2 gyroid units. The general trend of mechanical properties decreasing with increasing porosity was predicted by FEA, but manufacturing defects, as low relative density, caused differences ranging from 30 to 56 % between simulation and experiments. The difference between simulation and experiments increased with increasing relative density. No reference is made, however, to the selection of the 2x2x2 gyroid units model and its possible influence on the simulation results.

A procedure to build and validate a finite-element model for additively manufactured metal lattice structures has been described by [49]. They applied the method for face-centered-cubic and modified octet-truss lattices and showed average errors for the modulus and yield strength of 9-11% and 18%, respectively. Their study is comprehensive regarding the FEA because they analyze the influence of element type (beam elements versus solid elements) and finite element size. They also conducted a sensitivity analysis regarding the number of unit cells stacked together for the simulation and the effect of boundary conditions and material models. Finally, they also depict the increasing deviation between simulation and experimental results with increasing relative density.

Many authors perform FEA analysis on different porous structures and materials without investigating the RVE size. [24] analyses tantalum scaffolds using a 5 mm diameter by 5mm height model for the simulation. [41] uses a model about half the size of the compression sample.

A different approach for the simulation of gyroid TPMS implants is to assemble the implants in a material with the properties of the trabecular bone. For example, [36] divided the scaffolds into two halves; one was embedded into the cylinder base.

The bottom of the cylinder base was immobilized, and a vertical force was applied on top. Finding the stress shielding effect was notably reduced in the TPMS-based porous structures.

To overcome the manufacturing limitations of the Electron Beam Melting technology, which are similar to those of the SLM, [59] proposed using a reduced strut diameter for the simulations compared to the strut diameter used for the AM process. Using this reduced diameter allowed them to increase the accuracy of the simulations to predict the mechanic behavior. Initially, when the actual strut diameter was used for the simulations, the stiffness of the simulations was considerably higher than the one from the experiments. This same discrepancy has been described in the SLM method as unit cell size decreases and relative density increases [74].

2.2.4. Homogenization

Continuum mechanics is based on the concept of a homogeneous continuum material. However, all materials are heterogeneous if a sufficiently small scale is used. Generally, the homogeneous continuum assumption is no longer valid in composite and porous materials. Therefore, some artificial homogenization must be performed to use the continuum mechanics approach on composite or porous materials [7].

The main idea behind homogenization is that the mechanical behavior of the discontinuous material is somehow extracted from a small piece of porous material that FEA can easily simulate. This mechanical behavior is usually extracted as a stress-strain graph for uniaxial behavior or as a tensorial constitutive relation called material law for more general load cases. The stress-strain relation can be used to perform the FEA in macroscopical pieces of porous material without considering the microscopical porosity, just modeling as a continuous solid and using the constitutive behavior obtained from the porous model to account for its stress-strain behavior without considering its porosity at all, considerably lowering its computational expense.

Various analytical or computational homogenization techniques exist, from micro to macro. Homogenization models, also known as micromechanics models, can be classified into empirical, semiempirical, analytical, and numerical [6]. The last two would be considered further since they do not require experimental adjusting factors.

Analytical methods are also referred to as mean-field methods. Initial representatives of this class of methods were proposed before the advent of computers. Some analytical homogenization techniques are the Reuss Model, the Voigt Model,

and the Periodic Microstructure Model, which uses the Fourier series to estimate all the components of the stiffness tensor of a composite. These analytical methods are used to solve the inclusion and inhomogeneity problems, as reported by Eshelby in 1957 [75]. With the advantage of not being restricted to periodic material structures, constant stress or strain, periodic boundary conditions, or linear constitutive laws [14]. The Mori-Tanaka mean-field scheme considers the interaction between the embedded inclusions [7]. The main disadvantage of these methods is that they only allow relatively simple microstructural features to be modeled. However, they remain a current research topic [62], especially in tandem with the FE method [8]. The microstructure characterization through Micro-Computed Tomography (μCT) scans is used by [63] as an input for a two-step mean-field method to compute the effective elastic behavior.

On the other hand, computational homogenization methods comprise FE, fast Fourier transform methods, finite volumes, and finite differences, among others [7].

According to [46], in order to perform a direct computational homogenization, it is required to:

1. Define the RVE geometry and materials (the constitutive behavior of the individual constituents must be known).

2. Formulate the microscopic boundary conditions.

3. Calculate the microscopic output variables from the analysis of the deformed microstructural RVE (usually performed by the FE method).

4. Obtain the relation between the macroscopic input and output variables.

The formulation of the boundary conditions will be explained in section 2.2.5. First, the FE method is used to calculate the stress-strain relations for the RVE (step 3), then it is necessary to relate them to the properties of the macroscopic material (step 4). To that effect, it is assumed that the average mechanical properties of the RVE and the average properties of the composite are equal.

As derived in [70], parting from the average stresses and strains for the RVE, using Gauss's theorem and considering that the average strain in the RVE can be expressed as an integration around the boundary surfaces. They start from a parallelepipedal RVE under multiaxial loading and consider the assumption that stress distributions at the boundaries must also satisfy the periodicity condition. This periodicity condition means two corresponding points on two opposite planes with the exact in-plane coordinates must have the same normal and shear stresses). From that, it is possible to conclude that the average stresses in the RVE can be obtained from the resultant reaction forces on the boundary surfaces divided by the areas of the corresponding boundary surfaces.

Calculating the average stress as the division between reaction forces by boundary surface area can only be done if the adequate PBCs are applied to each pair of opposing nodes and the deformed boundary surfaces can distort and no longer remain plane, which is implemented by [45] in an open-access plug-in called EasyPBC. This plug-in can be installed into Abaqus CAE and automatically applies the required constraint equations, displacement boundary conditions, and estimates the homogenized elastic properties using the unified periodic RVE homogenization method described above. A cell periodicity node is included in COMSOL Multiphysics to perform the same homogenization for six load cases.

Computational homogenization is used by [16] to consider hexagonal-shaped composites as Cosserat continuum to perform their homogenization. Computational homogenization is also used to analyze fully coupled multiphase flow in deformable heterogeneous porous mediums [33] and to analyze the constitutive behavior of 3D printed parts enabling tailoring of the mesostructure to obtain the desired properties of the printed parts eliminating the expensive and tedious experimental work required to estimate the elastic moduli of printed parts [55]. The strain energy-based homogenization method is used by [42] to achieve a general multiscale topology optimization method for lightweight lattice structures obtained through additive manufacturing technology. [36] proposes an approximate homogenization method to achieve a constitutive description of small volume fraction particle-reinforced hyperelastic composites.

Artificial neural networks have also been used to replace the material model, and it has been found that they can achieve lower computation while being more general than analytical models to model constitutive behavior [58]. The results from computational homogenization of RVEs of composite materials have been used to train ANNs to produce their constitutive behavior [37] and could be used in the same way for porous materials like titanium bone replacement implants.

2.2.5. Representative Volume Elements (RVEs)

According to [45], the term RVE was first employed by [29] and can be defined as the smallest material volume of a composite material which can still represent the macroscopical behavior of the material. In other words, an RVE is a material volume whose effective behavior represents that of the material as a whole [1]. Figure 2.2 shows a typical example of a RVE, the unit that repeats itself is the small prism with the cylindrical fibers, the quarters of a cylinder on the corners become a full cylinder once the repetition is performed.

Figure 2.2 also shows an example of the selection of RVEs for this composite material. All three are equivalent, which means that they should all lead to

identical homogenized properties after homogenization.
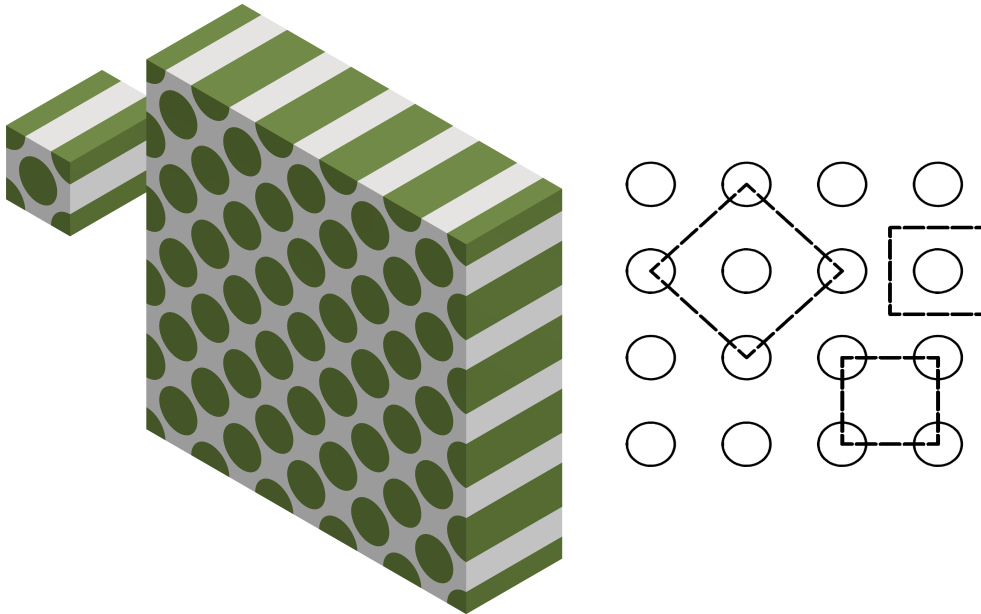
Figure 2.2.: Equivalent RVE selections to represent the same material.

Since the RVE homogenization method can analyze general geometries and nonlinear materials is suitable for investigating hyperelastic materials [25].

In RVEs, the microstructure is approximated as periodic. Moreover, even though most microstructures in engineering materials are non-periodic, the RVE concept has been vastly employed to model micro-structured materials, for example, non-porous solids (polycrystals and matrix inclusion composites), crystallographic microstructures [61, 17], and biological materials [11, 12]. An RVE composed of neurons (fibers) embedded in an extracellular matrix was used by [32]. In that study, isotropic visco-hyperelastic material properties were considered to study the loads, load rates, and neuron volume fraction impacts on the mechanical response of RVEs. In the porous solids field (fabrics, agglomerates, aggregates), RVEs are commonly used to study metal foams [34].

2.2.6. PERIODIC BOUNDARY CONDITIONS (PBCs)

PBCs must be created for the RVE so that the composite deformation is the same as the deformation of the RVE, and separation or overlap between neighboring RVEs is avoided.

Once two nodes have been identified as being associated (located at the ex-

act coordinates on opposing sides), the appropriate boundary conditions must be applied according to the type of constant strain being considered. For the average stress of the RVE to be equal to the reaction forces of a boundary surface divided by its area, the surface must be able to distort no longer remaining plane [70], which can be achieved if adequate PBCs are applied to each pair of opposing nodes of the FE analysis mesh, which implicates the geometry and the mesh intersecting the RVE boundaries in any opposing faces must be the same.

As previously mentioned, in RVE homogenization, the strain is uniformly applied in different independent sets of displacements, each set calculating a specific elastic material property, for example, if a uniform strain is applied to the x_1-direction, then the component of the Young's modulus obtained from that would be E_{11}, the Poisson's ratios ν_{12} and ν_{13}. [45] formulates for different uniform strains, and [70] shows the general tensor notation. For the constant strain in x_1-direction, applied to obtain E_{11}, the following BCs hold:

$$X_{Front} - X_{Back} = \varepsilon \tag{2.2}$$

$$X_{Top,Left} - X_{Bottom,Right} = 0 \tag{2.3}$$

$$Y_{Top,Left,Front} - Y_{Bottom,Right,Back} = 0 \tag{2.4}$$

$$Z_{Top,Left,Front} - Z_{Bottom,Right,Back} = 0 \tag{2.5}$$

Where X, Y, and Z are the displacement components (in x, y, and z-direction, respectively) of arbitrary nodal points, the subindex indicates the boundary surface which comprises them. The assigned strain value (ε) in Equation (2.2) is the only displacement degree of freedom that is constrained.

All the rotational degrees of freedom for the front and back surfaces are not constrained. Figure 2.3 helps explain those boundary conditions. For example, for points c and d located at opposed positions in the top and bottom surfaces, respectively, their displacements in x (blue), y (red), and z (green) directions must cancel each other according to Equation (2.3), Equation (2.4) and Equation (2.5). The same thing applies for points f and e located on the right and left surfaces, respectively. Finally, for points a and b located on the front and back surfaces, their displacements in y and z cancel out. However, their x displacements do not cancel out; instead, they correspond to the assigned strain value as indicated in equation Equation (2.2).
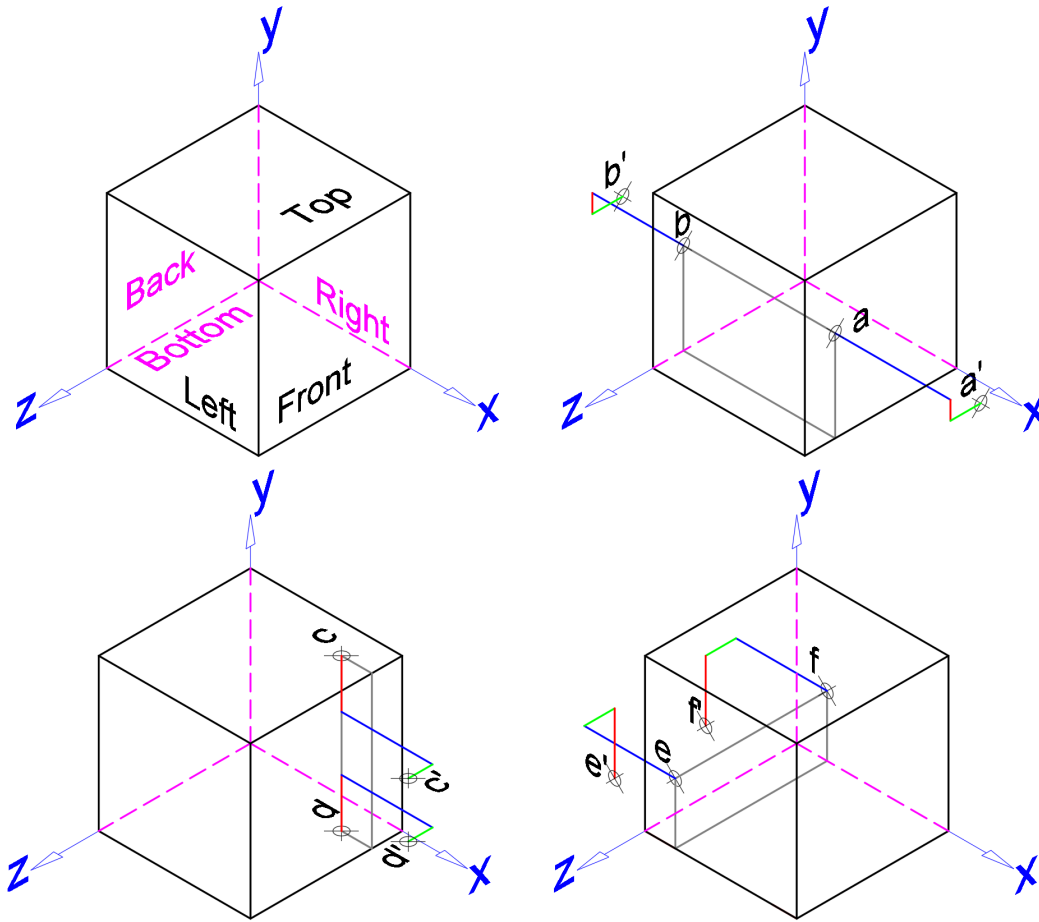
Figure 2.3.: PBCs for uniaxial strain in the x-direction.

2.3. Aim of this thesis:

Despite the abundant literature about the FEA simulation of gyroid Ti-6Al-4V additive-manufactured materials, the procedures to select the boundary conditions, plasticity models, and strain hardening models are not reported. Also, using the parameters and models from periodic structures for determining the adequate size of the RVE of Voronoi (stochastic non-periodic) Ti-6Al-4V additive-manufactured materials for simulations is not reported.

This thesis aims to perform simulations on RVEs of a triple periodic gyroid architecture of Ti-6Al-4V additive-manufactured material with different relative densities and to determine which plasticity models and parameters best represent the non-linear constitutive behavior and elastic modulus of the compression test specimens and provide the best computational performance. Afterward, this infor-

mation will help determine the optimal RVE size of the non-periodic Voronoi architecture with five different relative densities by comparing them with the uniaxial compression test results. These results will later be used to create homogenized material models for selected architectures and relative densities and implement them as user-defined material models in COMSOL Multiphysics.

3. Methods

3.1. Geometry Generation

The triple-periodic gyroid geometries and the Voronoi geometries are generated in the software nTopology (nTopology, Inc., New York, USA, [44])This software is an implicit modeling engine. Implicit modeling is a unique and lightweight way of representing three-dimensional objects using a single mathematical function to describe a solid body. In implicit modeling, every solid body is described by a single mathematical equation. This approach to solid modeling delivers considerable and sustainable advantages in reliability, speed, and scalability.

Taking advantage of this fast scalability, the focus of the geometry generation was on a specific strut thickness. Increments of 25 μm were considered until a final 0.3 mm strut thickness was obtained. The thinnest thickness manufacturable with the SLM was deemed to be 0.2 mm, so this was selected as the starting point.

The study began with a triply periodic minimal surface (TPMS) gyroid block. The unit cell size was changed progressively for each strut thickness until the desired relative density was obtained. Table 3.1 shows the unit cell sizes obtained by this process with their respective relative density and strut thicknesses. Each of the relative densities represents a distinctive material characterized by simulation. Compression tests were performed for samples of each relative density.

The gyroid architecture is constructed over the basis of a unit cell repetition. Figure 3.1 shows the graphical representation of the unit cells of gyroid structures once the volumetric mesh has been generated in nTopology and imported into COMSOL Multiphysics. It can be seen how the wall thickness increases with increasing relative density. On the contrary, the unit cell size (the repeating unit) is reduced as the material's density increases. The unit cell model was used for the simulations, but the actual RVE size corresponds to 2x2x2 unit cell sizes due

Table 3.1.: Relative density, unit cell, strut thickness, and porous size of gyroid porous architectures

Relative density	Porous Size [μm]	Unit Cell Size [mm]	Strut thickness [mm]
0.1	1230	3.860	0.200
0.2	610	2.170	0.225
0.3	470	1.616	0.250
0.4	290	1.339	0.275
0.5	209	1.173	0.300

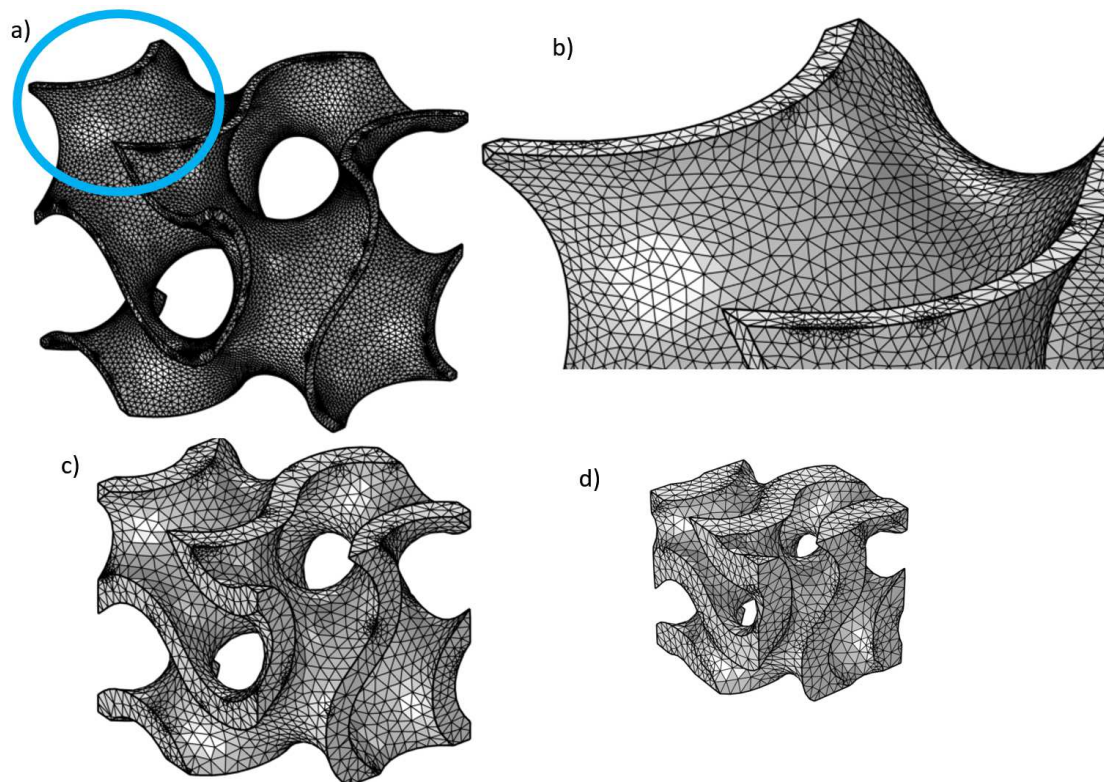to the employed boundary conditions.

Figure 3.1.: Unit cells for the triply periodic gyroid structure a) 0.1, c) 0.3, and d) 0.5 relative densities with the same scale after volumetric mesh generation in nTopology; b) shows a detailed view from a) at a larger scale.

Figure 3.1 a) and b) show how the meshing algorithm from nTopology, used

microscopic elements to incorporate tiny geometry details; these more minor elements in nTopology also appeared after the import and mesh generation process in COMSOL Multiphysics.

The size ratio between mesh elements is an essential measurement of mesh quality. Tiny elements combined with significant elements caused convergence problems when performing the FEA analysis. The small mesh elements shown in Figure 3.1a) did not cause problems with the 0.1 relative density since the wall thickness was small. Therefore, the meshing algorithm was not obligated to use extensive elements to mesh the strut, causing the mesh elements to have a relatively similar size (the size ratio between elements was not excessively low).

As the relative density increased (Figure 3.1 c) and d)), the unit cell size decreased, but the wall thickness increased, and the meshing algorithms used more significant elements to mesh the thicker walls, and their coexistence with the tiny elements created convergence problems. Using constant values of 0.07 mm for the element size and 0.01 mm for the minimum element size during the meshing in nTopolgy proved adequate for all of the densities of the gyroid family.

The geometries in nTopology are not conventional 3D solids with edges, surfaces, and volumes. Instead, the implicit modeling approach creates a graphical rendition of a mathematical function. The implicit modeling allows instant modifications of the architecture or geometry of interest by changing the inputs to the geometry-defining function or the function itself. This capability of instant changes in the architecture and size of the microstructure of the materials would be virtually impossible to replicate in a conventional CAD approach for modeling this type of micro and mesostructured materials.

As soon as the desired architecture was finally chosen, it was time to export the resulting material samples for fabrication or simulation. Creating conventional solids from the implicit models in nTopology for direct simulation in COMSOL Multiphysics was impossible. Instead, a volumetric mesh was created from the implicit model in nTopology and was successfully imported and used in COMSOL Multiphysics to perform simulations.

The repetition of the cubic unitary cell of 3.860 mm of the gyroid of 0.1 relative density in 3D space creates the architected porous material. The desired volume and shape are specified. The intersection between the infinite material and the specified volume obtains the desired part. For example, the compression sample of 12 mm in diameter is shown in Figure 3.2.

The geometry generation is slightly different for the stochastic Voronoi architectures. No unit cell can be repeated volumetrically to create the macroscopic material. Instead, a random set of points is generated for the complete geometry
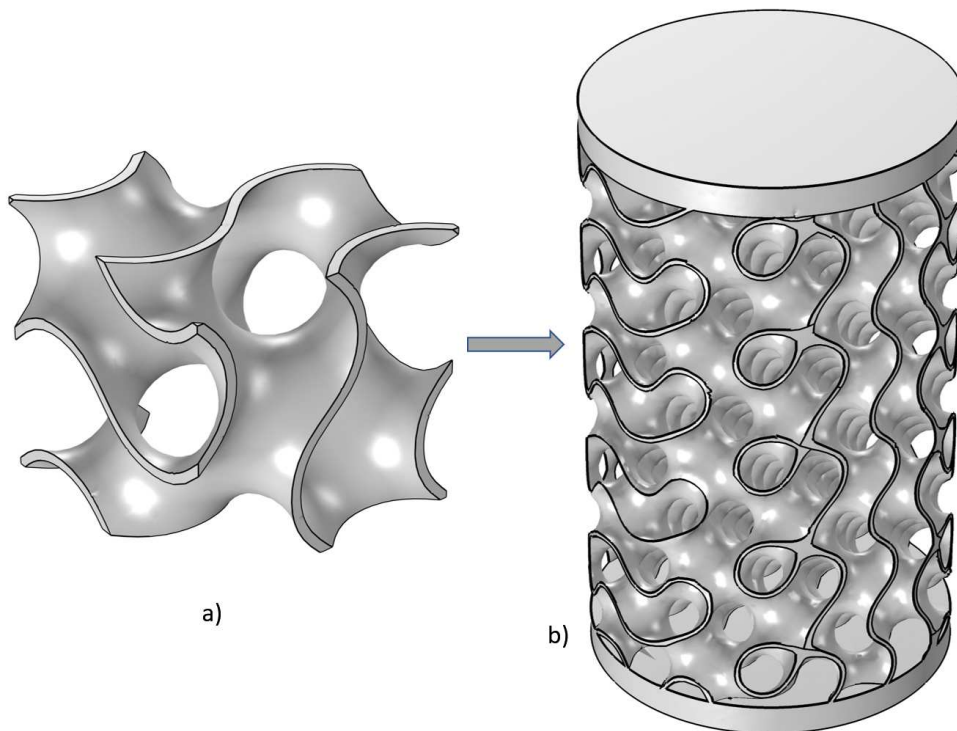
Figure 3.2.: a) Gyroid unit cell of 0.1 relative density and b) compression sample built with the same parameteres

of interest, e.g., a simulation cube, a compression test specimen, or an actual bone replacement part. For this type of stochastic structure, the size of the RVE, which represents the material's properties as a whole, has to be determined experimentally by simulation.

Figure 3.3 shows an RVE of stochastic Voronoi architecture of 0.1 relative density and a compression sample. Both were built with the same average point spacing and strut thickness; therefore, both have the same relative density. However, the compression sample model is in no way a periodic repetition of a unit cell. The concept of the unit cell is invalid in this type of architecture.

nTopology uses the Voronoi cell boundaries as the axis for the solid struts, while the Voronoi cells remain void. Struts of a specific size are used; however, at points where several cells intersect, the thickness can be increased depending on the random seed used; therefore, a large enough RVE must be used to represent this kind of random variation adequately.

The average point spacing was modified progressively for a given strut size until the desired relative density was achieved. As the relative density increases,
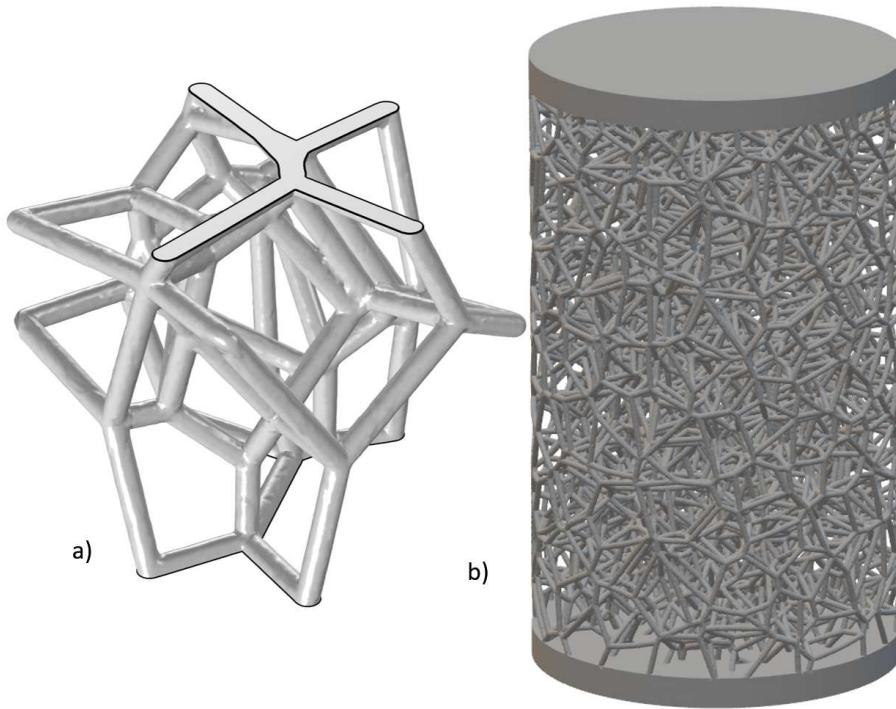
Figure 3.3.: a) RVE of stochastic Voronoi architecture of 0.1 relative density and b) compression sample model built with the same parameters.

the average point spacing decreases. Table 3.2 shows the average point spaces, which result in the relative densities of interest for the given strut thicknesses.

Figure 3.4 shows RVEs of the Voronoi architectures for different relative densities. For compression tests, the samples of all the relative densities had the same size, but for simulation purposes the RVE size startet with the smallest size possible. The RVE size was progressively increased until the simulation results mimicked the strain-stress behavior of the compression tests.

The relative densities and strut thicknesses of the gyroid and the Voronoi families are comparable, which allows for a direct comparison of the effectivity of both architectures to mimic the human bone's Young's modulus with the maximum yielding strength possible.

After the complete sample models were created in nTopology $.3mf$ 3D manufacturing format files were generated and used for additive manufacturing by SLM. After the fabrication, the samples were heat-treated to reduce manufacturing stress, and finally, the uniaxial compression tests were performed. Figure 3.5 shows one batch of test specimens recently extracted from the SLM build chamber, and Figure 3.6 shows an example of a Voronoi architecture RVE of 0.1 relative

Table 3.2.: Relative densities of Voronoi architectures

Relative density	Av. Point spacing [mm]	Strut thickness [mm]
0.1	1.511	0.200
0.2	1.133	0.225
0.3	0.977	0.250
0.4	0.889	0.275
0.5	0.829	0.300
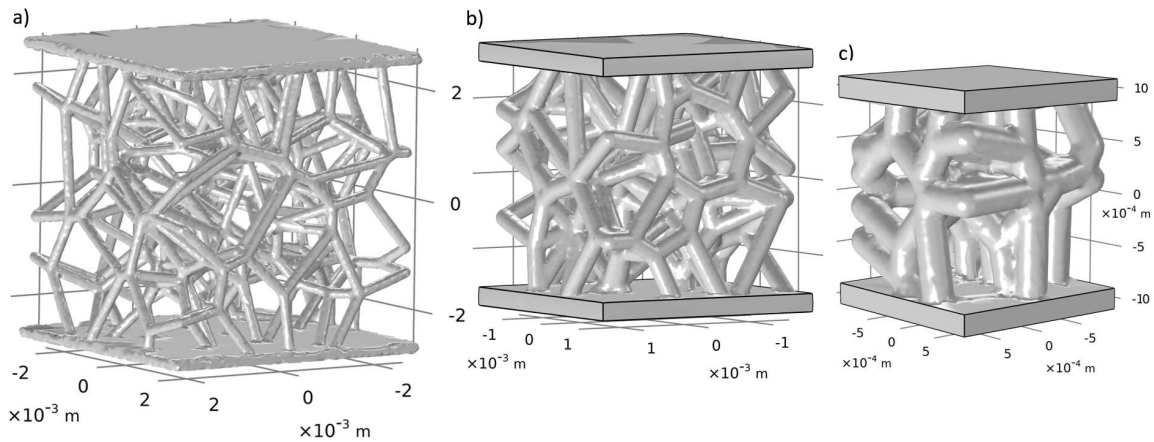
Figure 3.4.: Simulation RVEs for Voronoi architectures of a) 0.1, b) 0.3, c) 0.5 relative densities

density and one compression sample of this same relative density.

The location of the samples of different architectures and densities in the SLM bed was randomized to counteract any possible influence of it over the quality of the manufacturing process. Three compression test samples of each relative density were manufactured and tested.

The material used was powdered Ti-6Al-4V ELI (Grade 23) Titanium from SLM Solutions (Lübeck, Germany) [53]. With a spherical particle size of 30 μ and a density of 4.43 g/cm^3. The material properties for the sintered material from the material data sheer are offset yield strength of 887 MPa and Young's modulus 126 ± 1 GPa considering a test direction parallel to the additive manufacturing direction. The manufacturer does not report the Poisson's ratio; a value of 0.33 was used for the simulations.

The SLM machine was an SLM-280. The compression tests were performed

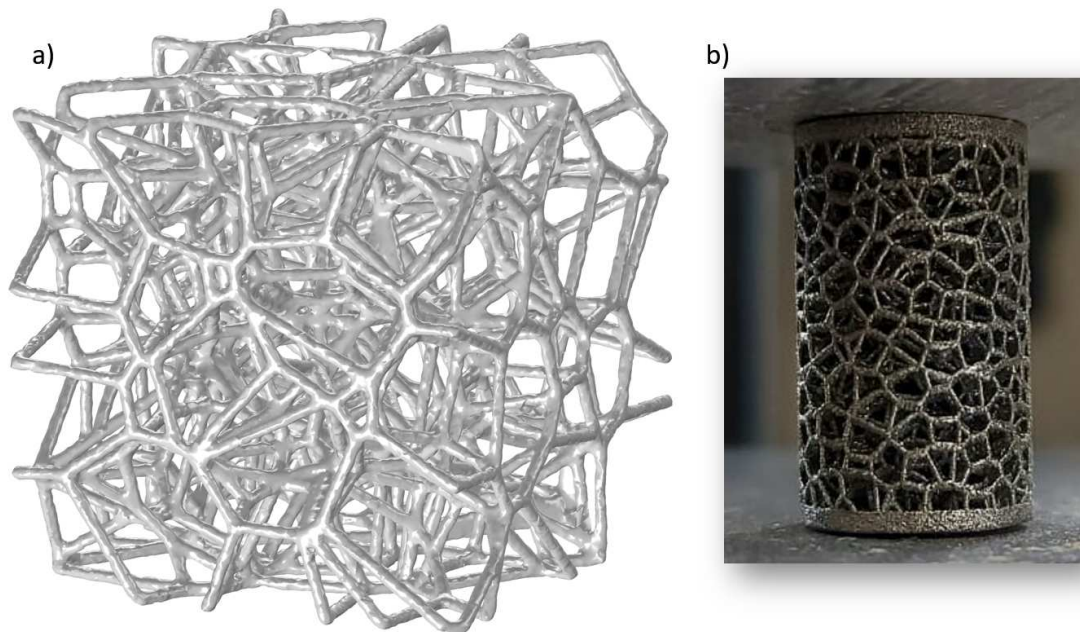**Figure 3.5.:** DLMS fabricated compression and fatigue test specimens [2]

Figure 3.6.: Stochastic Voronoi architected material of 0.1 relative density a) cubic model of 5x5x5 mm and b) as built cylindrical 12 mm diameter compression sample [2].

in a Universal System Machine Zwick 100 kN. The strain rate used was 0.10-2 s^{-1} under the standard ISO 13314 mechanical testing of metal's ductility testing compression test for porous and cellular metals. The manufacturing of the SLM samples and the mechanical tests were performed as part of the doctoral project of M.Sc. Miguel Araya-Calvo and the collaboration between the Costa Rica Institute of Technology and the Future Manufacturing Technologies (FMT) research group of the University of Oulu, Finland.

3.2. FEA MESH GENERATION.

A procedure was developed to set up the FEA mesh in COMSOL Multiphysics. First, the *.3mf* file containing the mesh generated in nTopology was imported. Then, a solid was generated from this imported mesh. Afterward, the generation of a native COMSOL Multiphysics was attempted. When no errors appeared, and the mesh metrics were acceptable, the setup for the simulation was continued. On the contrary, when errors appeared during the native mesh generation, which did not clear with mesh refinement, it was necessary to perform mesh operations in the mesh tab, mainly joining operations, but sometimes boolean and partitions. These mesh operations are performed directly on the imported mesh part, so after them, the solid must be rebuilt, and the native COMSOL mesh is again created, most often clearing the previous cases.

COMSOL Multiphysics has various importing capabilities for different mesh file types. In the same way, nTopology can export volumetric meshes in various formats. After some testing, *.3m*f and *.stl* file formats were successfully imported to COMSOL Multiphysics. For standardization reasons, the *.3mf* was selected as the export file type from nTopology for the rest of the present study.

Imported mesh data can be used in two ways: directly as a mesh for analysis or indirectly as a geometry object. Creating a geometry object is generally more convenient because planar faces can be recognized and used to create suitable boundary conditions. Figure 3.7 a) shows the result of importing the mesh generated in nTopology into COMSOL Multiphysics. The imported mesh is too refined, causing significant computation times. Therefore, it is more convenient to create a solid from it and then mesh it directly in COMSOL Multiphysics using the recommendations for structural mechanics simulations corresponding to tetrahedral quadratic serendipity finite elements. Figure 3.7 b) and c) show the solid and the new mesh with more prominent elements more suitable for lower computation times.

Importing the *.3mf* file was done in the Geometry toolbar, browsing for the corresponding file. The *Simplify mesh* and the *Form solids from surface object*

options are selected by default. The *Relative simplification tolerance* includes two options: *Relative simplification tolerance* and a *Defect removal factor* set by default to be 0.01 and 1, respectively. Less simplification of the mesh is performed when those two values are decreased. On the other hand, raising the Relative simplification tolerance and Defect removal factor fixes more issues in the mesh, although it may result in a less accurate representation of the imported surface mesh.
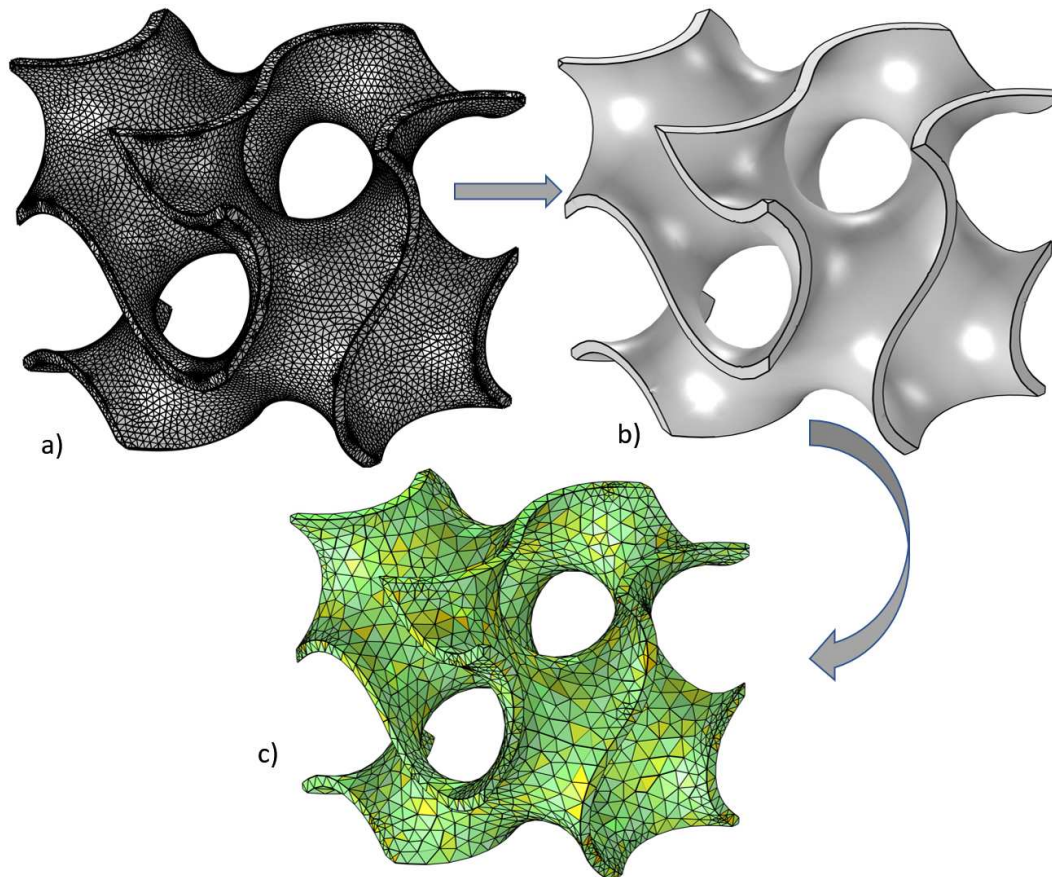
Figure 3.7.: Imported nTopology geometry in COMSOL Multiphysics, a) as imported mesh object, b) derivated solid, and c) new mesh created in COMSOL Multiphysics and evaluated concerning mesh quality.

While importing the geometries into COMSOL Multiphysics, it was common to encounter problems, especially during the new mesh generation. The more frequent errors were self-intersections and insufficient minimum element size to incorporate small details from the imported mesh. Changing the Relative simplification tolerance and the Defect removal factor did not solve the mesh problems. Decreasing the element size for the meshing from normal to fine was sufficient

for the gyroid geometries but not for the stochastic geometries, which required a joining operation.

Figure 3.8 shows a sample Voronoi geometry after it has been built using the default importing settings. The black lines visible when struts intersect become a problem when creating the new simulation mesh in COMSOL. Due to their small size, when the meshing algorithm tries to incorporate them, it must refine the grain size significantly, which causes mesh quality problems. When the mesh quality is poor, the computational time increases, and sometimes convergence is not achieved in the solution. On other occasions, the mesh algorithm is unable to mesh the part. Therefore, performing a procedure to remove these intersection lines was vital. It can be achieved by creating a Join operation in the Mesh Parts section of the Model Builder.
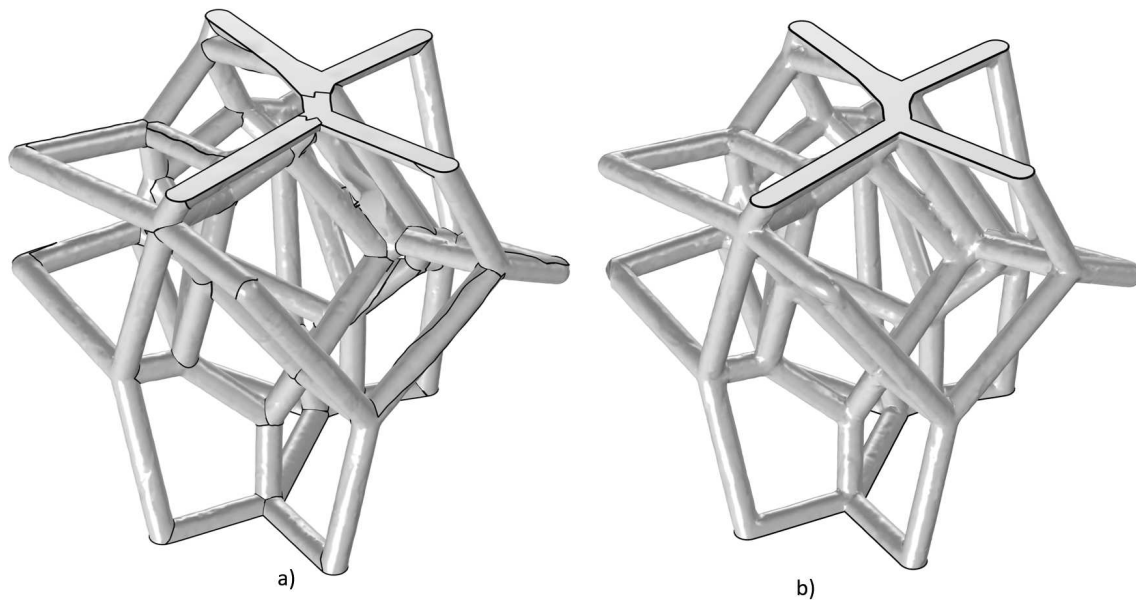
Figure 3.8.: Voronoi architecture of 0.1 density a) before and b) after the joining operation.

The result of performing the Join operations is shown in Figure 3.8. Afterward, the new mesh is generated in COMSOL Multiphysics. This procedure can substantially improve the quality of the mesh. Table 3.3 shows the effect of the joining operation on the mesh quality. Even though there is an increment in the number of finite elements due to the joining operation, and the average element quality did not improve considerably, the minimum element quality was improved by 556%. The FEA simulation did not converge before the joining operation but did afterward, highlighting the importance of this step.

Table 3.3.: Effect of joining operation in mesh quality

	Before joining operation	After joining operation
Number of elements	41925	43780
Minimum element quality	0.0215	0.1198
Average element quality	0.6542	0.6632

COMSOL Multiphysics allows the user to select the quality measure between Skewness, maximum angle, volume versus circumradius, volume versus length, condition number, and growth rate. The skewness measure is suitable for most meshes; hence, it is the default measure. This quality measure is based on the equiangular skew that penalizes elements with large or small angles compared to the angles in an ideal element. This quality measure is also used when reporting bad element quality during mesh generation.

The effect of the joining operation on the mesh skewness measurement can be seen in Figure 3.9. The finite elements from Figure 3.9 a) possess a lower quality, evidenced by the higher number of orange and red elements. Also, the size and shape of the triangular elements appear to be less uniform before the joining operation is performed. It is also evident in Figure 3.9 b) how the joining operation causes features from the original mesh to be approximately represented, but the gains in computing time are considerably more critical. Besides, the limitations of the manufacturing process also prevent the manufactured material from incorporating those tiny features from the original n-Topology mesh.

As mentioned before, when importing a mesh or 3D printing file, it is optional to simplify the mesh before creating the geometry. The simplification can remove minor defects typically present in mesh data from measurements, such as tomography, and it can speed up geometry processing by removing unnecessary elements from all meshes. The Simplify mesh option has two parameters that can be modified. The *Relative simplification tolerance* is relative to the dimensions of the entire geometry and specifies a global limit for how much the mesh can be modified. The *Defect removal factor* is relative to the local feature size, as estimated by the algorithm, and is combined with the global limit to produce a limit for how much the mesh can be modified at a particular location. If the mesh contains many defects that must be removed, the value of the *Defect removal factor* can be increased. If the mesh describes the desired geometry with high accuracy, it might be possible to decrease this factor instead. Changing both parameters was investigated while trying to correct mesh problems. However, the results were hard to standardize and required much trial and error. It was found more efficient
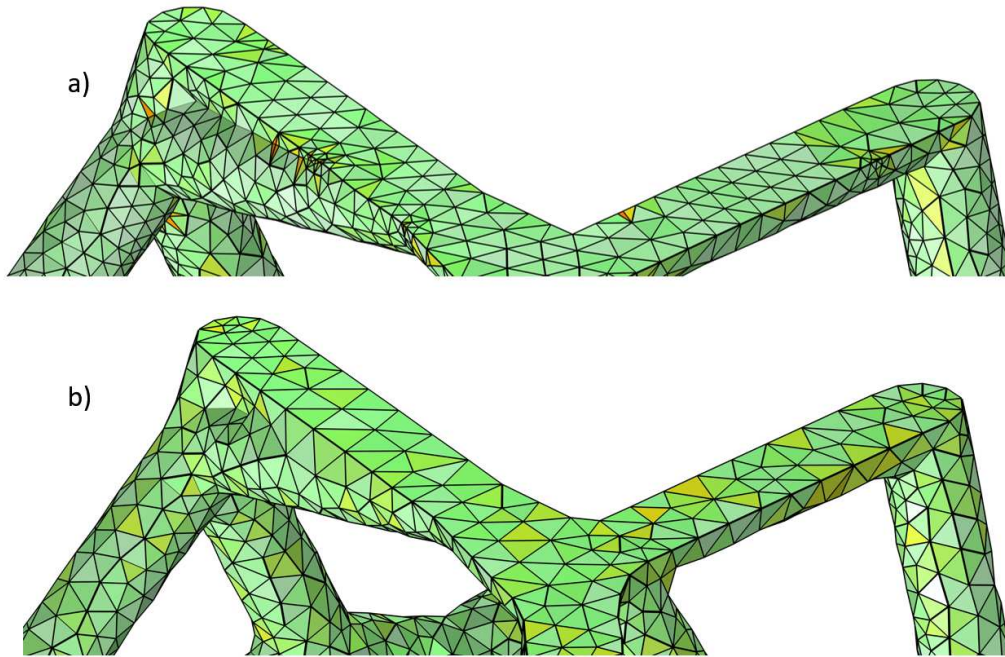
Figure 3.9.: COMSOL Multiphysics mesh quality measured by skewness a) be-
fore and b) after performing the joining operation. A skewness of
one is the optimal value.

to modify the meshing parameters in nTopology and import the mesh with the
default parameters afterward, performing the joining operation when necessary.

3.3. BOUNDARY CONDITIONS.

Different possibilities for boundary conditions can be used to simulate a compres-
sion test. First, deciding between applying a prescribed force or a displacement
is necessary. When a prescribed force is used, it is necessary to determine the
magnitude of the force sufficient to cause yielding on the sample, which can be
more cumbersome because the area of the sample must be considered.

In this study, it was decided to prescribe displacement instead of force. Once
a specific strain is selected for the simulation of a sample, it is straightforward
to replicate the same strain on a different size sample because the relationship
between the size of the sample and a specific strain is always linear.

Usually, real-life compression tests are performed, as shown in Figure 3.11, by
placing the sample between the compression test machine plates without any addi-

tional constraints. Similarly, the compression test simulation can also be performed
by placing the sample between plates considered rigid bodies. That approach be-
comes helpful when considering models without plane faces that can be selected
to apply a prescribed displacement. However, using rigid plates for the simulation
requires the activation of a contact formulation between the plates and the sample;
this adds more complexity to the model and can increase the computation time.

On the other side, it is common to employ the flat surfaces of solid models
to apply boundary conditions such as prescribed displacements, symmetries, and
forces or pressures. As shown in Figure 3.10, it was possible to create 3D solids
with planar boundaries, which facilitates the introduction of boundary conditions
directly on the model without using rigid plates to compress the sample.
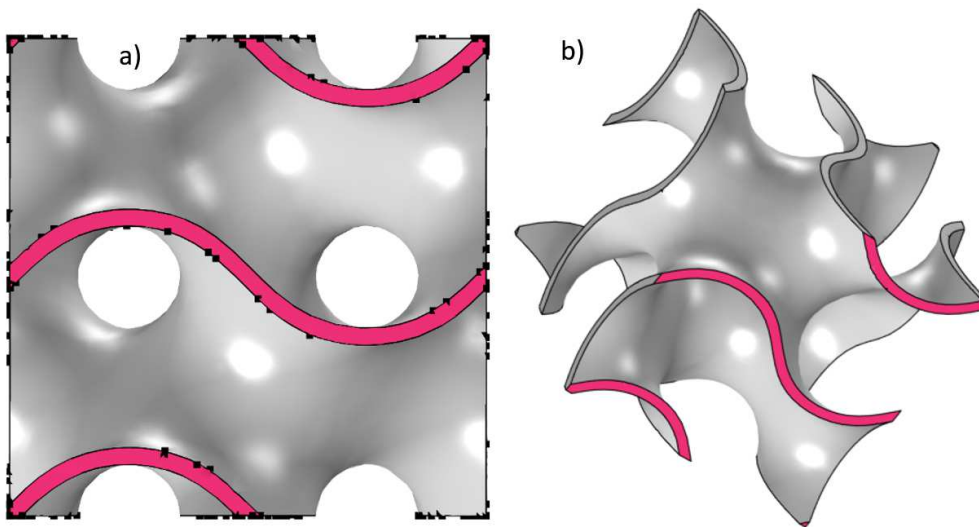
Figure 3.10.: Unit cell of gyroid architecture with 0.1 relative density, a) bottom
face view, the dots correspond to automatically generated points
which can be used for boundary conditions, b) isometric view

The friction force between the plates of the compression testing machine and
the sample is usually enough to keep the sample in place. Sometimes, additional
clamping is used to keep the sample in place, but it was not the case in the current
study. Theoretically, when no additional fastening devices are used, the sample
has only two restrictions to its degrees of freedom, e.i. z = 0 at the bottom and z =
strain in the top face. However, because of friction against the plates, the sample
has no apparent displacement in the radial direction, as seen in Figure 3.11 b).

When creating a simulation of the compression test, an option is to select the
whole bottom of the sample to be fixed to the ground, which removes all degrees of
freedom from it, an approach that is very common in the literature . Conversely, in

other authors, only one degree of freedom, the axial, is removed from the bottom and top faces, respectively. However, to perform the simulation with this approach, it is necessary to have at least one fixed point in the bottom face to prevent the sample's rigid body motion. This fixed point should be in the center of the sample because, in the case of a symmetric uniaxial compression load, this point has no displacement. The location of a point right at the center of the bottom face is not always possible (the RVE might be void in the center of the bottom face). Even when possible, additional effort is required to create a center point because, as seen in Figure 3.10 a), the automatically generated points do not necessarily coincide with the center of the face.
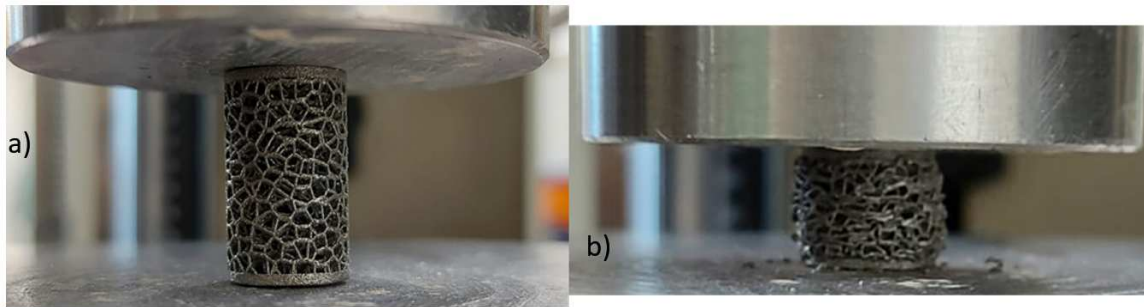
Figure 3.11.: Voronoi sample of 0.1 relative density a) before, and b) after compression test [2]

The easiest way to create a point right at the center of the bottom face is by using symmetry boundary conditions. The bottom corner between the left and right symmetries becomes the center of the bottom face of the sample. Therefore, all its displacements and rotations can be prescribed and equal to zero to avoid the rigid body motion problem. Figure 3.12 shows this approach for a gyroid sample of 0.1 relative density with the addition of two symmetry boundaries (green and purple).

The use of symmetry implies that simulation is performed in a sample four times larger than the model. When a homogenization of the RVE is not performed, as in the first part of this study, the use of a larger sample size is beneficial because its constitutive behavior is generally more representative of the material's behavior, as compared with using one unit cell only.

The main advantage of using the symmetry boundary conditions is that a larger material sample can be analyzed, but the computation effort is considerably lower than that of an equivalent volume sample without the symmetry boundary conditions.

In order to determine which approach to utilize, a comparison was performed

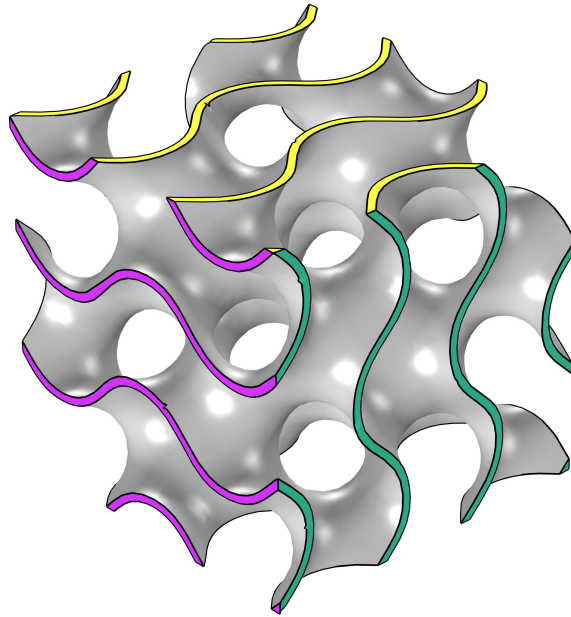**Figure 3.12.:** Symmetry boundary conditions for compression test simulation of gyroid material with 0.1 relative density. In purple, the left symmetry surface, in green, the right symmetry surface; and in yellow, the top face with a negative displacement in the z-direction. The bottom corner between the green and the purple faces is completely fixed. The bottom face only has a fixed displacement in the z-direction.

between a completely fixed bottom face and the already explained only-z prescribed displacement for the face and a unique fixed point. The latter was selected as the more advantageous, which will be presented in the results section.

RVEs of Voronoi stochastic materials are modeled differently. Figure 3.13 a) shows an RVE of Voronoi 0.1 relative density material. In this case, the top and bottom boundaries are selected so that struts intersect them roughly perpendicularly. Another approach was evaluated in which all struts, even the ones parallel to the top and bottom surfaces, were cut, generating plane faces that could be used for the boundary conditions, as seen in Figure 3.13 b). Symmetry boundary conditions are not possible for these two cases. Instead, a fixed boundary condition (restricting all degrees of freedom) had to be used for the bottom face.

Finally, the introduction of artificial plates at the top and bottom of the RVE was tried Figure 3.12 c). This final approach proved to render the most accurate simulations because it allows using symmetry boundary conditions similar to the

ones explained for the gyroid family.

The Voronoi materials are in no way a repetition of unit cells, and the use of symmetry boundary conditions implies the repetition of the RVE four times. A more exact material representation should be an RVE four times as large with no symmetric BCs. However, this implies a significantly greater computing effort. The accuracy of the simulations with these boundary conditions was sufficient. Therefore, it was decided that their advantages in simulation time were more significant than the accuracy loss due to mirroring the RVE two times with the symmetry boundary conditions.
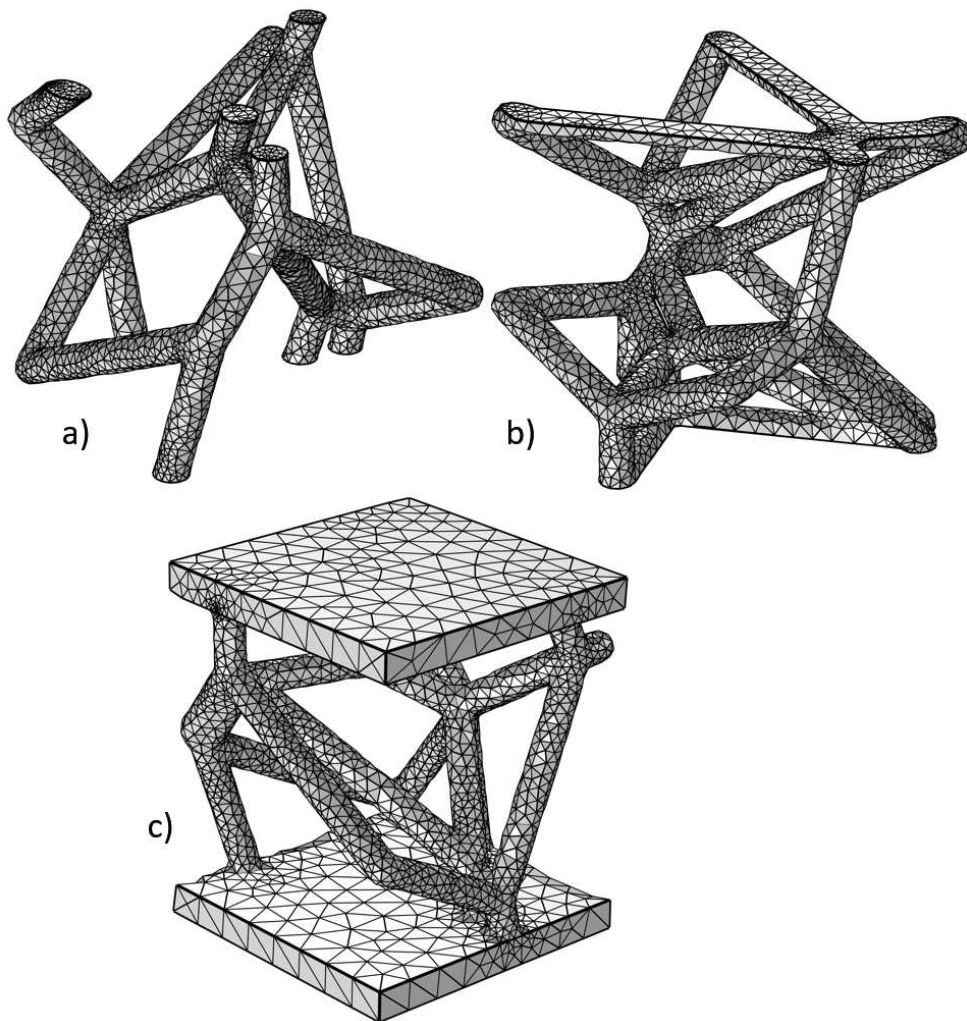

Figure 3.13.: Different implementation of boundaries for Voronoi structure of 0.1 relative density a) only struts, b) plane faces, and c) artificial plates.

It was found that an offset of the top and bottom plates from the Voronoi struts is beneficial. It is impossible to incorporate the strut shown in Figure 3.14 a) into the joining operation. The small distance between the strut and the plate's vertical face causes them to be created as a single entity during the import process. Further intersection operations could separate them, but they involve an additional effort and do not always work. Instead, a slight separation between the struts and the vertical face, as shown in Figure 3.14 b), avoids the consideration of struts and vertical faces as a single unit, saving considerable effort and time during the simulation setup. The use of this offset did not have a significant effect on the stress-strain results.
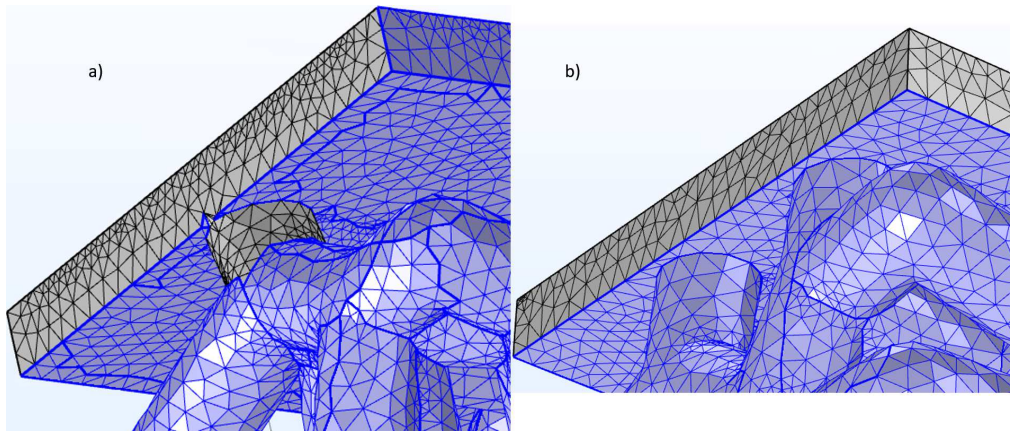
Figure 3.14.: Offset of top and bottom plates from Voronoi RVE a) no offset b) offset

3.4. Elasto Plasticity Model and Simulation setup

The heat treatment used by the powder manufacturer was the following: specimens were heated up in a vacuum atmosphere at a rate of 450 °C per hour up to 910 °C, then with 300 °C per hour up to 940 °C. Subsequently, they were held at 940 ± 10 °C for four hours. Cooling down in vacuum at a rate of 40 °C per hour to 760 °C, then in argon with 560 °C per hour to 480 °C, followed by gas fan quenching at any rate to 50 °C (SLM Solutions, 2022). Table 3.4 shows the datasheet of the powder material in the as-built and heat-treated conditions.

Table 3.4 also shows the anisotropy of the material's properties when tested vertically (parallel to the manufacturing direction) or horizontally (perpendicular

to the manufacturing direction). The values for heat-treated vertically tested properties will initially be used for the simulations of the porous materials.

Table 3.4.: Titanium Ti-6Al-4V alloy data sheet as reported by the manufacturer for DSLM. M : Mean; SD: Standard Deviation; H: Horizontally tested V: Vertically tested

		As-built		Heat-treated	
		M	SD	M	SD
Offset yield strength [MPa]	H	1076	30	851	12
	V	1170	26	887	12
Young's modulus [GPa]	H	113	1	120	5
	V	117	2	126	1

A compression test of a strut filament was not performed. Therefore Young's modulus of 126 GPa and yield strength of 887 Mpa were used to overwrite the COMSOL Multiphysics built-in Titanium beta-21 S properties for the initial simulations. Subsequent comparison with the experimental results allowed them to be updated to values closer to the actual additively manufactured porous architectures. The typical uniaxial stress-strain behavior of a ductile metal can be seen in Figure 3.15 a) the elasticity limit corresponds to the yield strength. Beyond this point, any subsequent deformation does not return to the reference configuration. Instead, it leaves a residual strain. Since the elastic limit is challenging to evaluate, the Offset yield is defined. The linear elastic portion is displaced to the right by 0.002 units of strain and plotted parallel to the original. The point where this line intersects the experimental curve is defined as the Offset yield strength (Figure 3.15 b).

COMSOL Multiphysics is a finite element analysis, solver, and simulation software package for various physics and engineering applications, especially coupled phenomena and multiphysics. For the current study, single physic Solid Mechanics simulations were created.

Linear elastic behavior is automatically added to the Solid Mechanics simulation with the selection of the built-in titanium material. An additional subnode is added to the Linear Elastic node to account for the plastic behavior. For the plastic behavior Plasticity, Porous Plasticity and no plasticity were evaluated.

After the plasticity behavior has been selected, it is necessary to use Large or Small Plastic Strain Theories. The Large Plastic Strain Theory uses a multiplicative decomposition of elastic-plastic strains and maintains the incompressibility
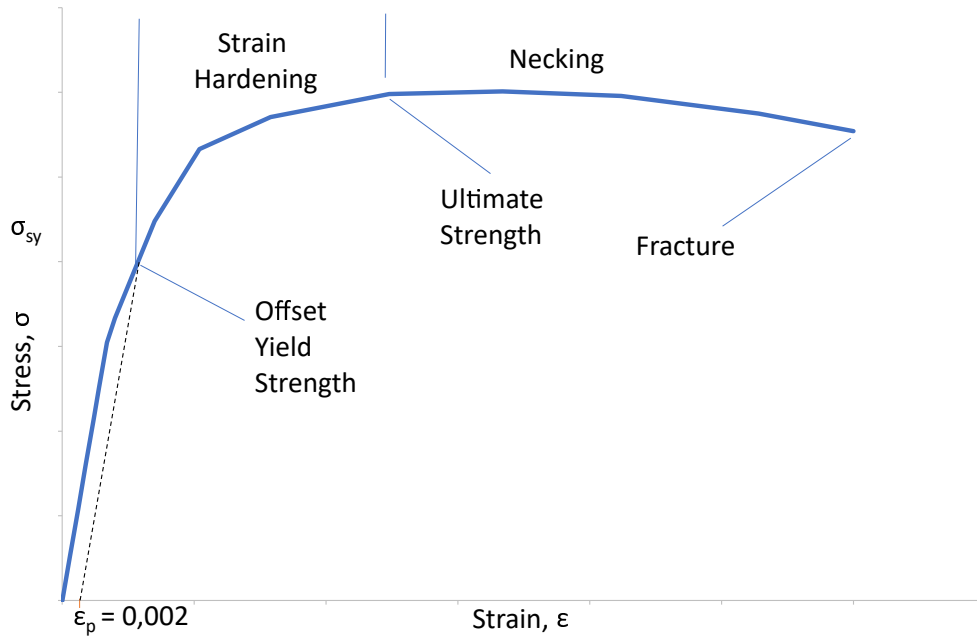
Figure 3.15.: Typical uniaxial stress-strain diagram for ductile material and off-set yield strength graphical calculation.

of the plastic deformation. The Small Plastic Strain Theory, also called Finite Plasticity Theory, performs an additive decomposition [30], which is less accurate but generally has fewer convergence problems. In the current study, the maximum strain used in the simulations was 8% which can still be considered negligible, allowing the use of the Finite Plasticity simplification.

The definition of the Yield Function is required for the plasticity and porous plasticity nodes. A yield criterion defines the stress condition under which plastic deformation occurs. Stress paths inside the yield surface result in purely recoverable deformations (elastic behavior), while paths intersecting the yield surface produce both recoverable and permanent deformations (plastic strains). When an associated flow rule is applied, the yield function must be smooth and continuously differentiable with respect to the stress. In COMSOL Multiphysics, the following form is used:

$$F_y \;=\; \sigma_e \;-\; \sigma_{ys} \tag{3.1}$$

Where σ_{ys} is is the yield stress, the scalar function $\sigma_e\,(\boldsymbol{\sigma})$ is the equivalent stress; σ_{ys} can be a constant (for perfectly plastic materials) or a variable for strain-hardening materials. The default form of the equivalent stress is the von

Mises stress, which is often used in metal plasticity:

$$\sigma_e = \sigma_{Mises} = \sqrt{3 \, J_2 \, (\boldsymbol{\sigma})} \tag{3.2}$$

The von Mises criterion suggests that the yielding of the material begins when the second deviatoric stress invariant J_2 reaches a critical value. This criterion can be written in terms of the elements of Cauchy's stress tensor

$$J_2 = \frac{1}{6} \left((\sigma_{11} - \sigma_{22})^2 + (\sigma_{22} - \sigma_{33})^2 + (\sigma_{33} - \sigma_{11})^2 \right) + {\sigma_{12}}^2 + {\sigma_{23}}^2 + {\sigma_{13}}^2 = \kappa^2 \tag{3.3}$$

or equivalently $\sqrt{J_2} = \kappa$ The von Mises criterion is implemented in COMSOL Multiphysics as

$$F_{y \; Mises} = \sqrt{3 \, J_2} - \sigma_{ys} = 0 \tag{3.4}$$

where σ_{ys} is the yield stress level (yield stress in uniaxial tension).

Tresca stress, Hill orthotropic plasticity, or a user-defined expression can be specified as the equivalent stress [18]. The von Mises and Tresca criteria are independent of the first stress invariant I_1 and are mainly used to analyze plastic deformation in metals and ductile materials. The von Mises and Tresca criteria belong to the volume preserving or J_2-plasticity, as the plastic flow is independent of the mean or hydrostatic pressure. The von Mises criterion was used for this study due to the Titanium alloy's ductile behavior.

3.4.1. ISOTROPIC PLASTICITY.

At most, the plastic potential Q_p is written as a function of three invariants of Cauchy's stress tensor for isotropic plasticity.

$$Q_P (\boldsymbol{\sigma}) = Q_P (I_1 (\boldsymbol{\sigma}) , \; J_2 (\boldsymbol{\sigma}), \; J_3 (\boldsymbol{\sigma})) \tag{3.5}$$

Where the invariants of the stress tensor are

$$I_1 (\boldsymbol{\sigma}) = trace \; (\boldsymbol{\sigma}) \tag{3.6}$$

$$J_2 (\boldsymbol{\sigma}) = \frac{1}{2} \left[(trace \; \boldsymbol{\sigma})^2 - trace \; (\boldsymbol{\sigma})^2 \right] \tag{3.7}$$

$$J_3 (\boldsymbol{\sigma}) = det \; (\; dev \; (\boldsymbol{\sigma})) \tag{3.8}$$

so that the increment of the plastic strain tensor $\dot{\boldsymbol{\varepsilon}}_p$ can be decomposed into

$$\dot{\boldsymbol{\varepsilon}}_p = \lambda \; \frac{\partial Q_P}{\partial \boldsymbol{\sigma}} = \lambda \; \left(\frac{\partial Q_P}{\partial I_1} \frac{\partial I_1}{\partial \boldsymbol{\sigma}} + \frac{\partial Q_P}{\partial J_2} \frac{\partial J_2}{\partial \boldsymbol{\sigma}} + \frac{\partial Q_P}{\partial J_3} \frac{\partial J_3}{\partial \boldsymbol{\sigma}} \right) \qquad (3.9)$$

The increment in the plastic strain tensor $\dot{\boldsymbol{\varepsilon}}_p$ includes in a general case both deviatoric and volumetric parts.

The trace of the incremental plastic strain tensor, which is called the volumetric plastic strain rate $\dot{\boldsymbol{\varepsilon}}_{pvol}$, is only a result of the dependence of the plastic potential on the first invariant $I_1(\boldsymbol{\sigma})$, since $\frac{\partial J_2}{\partial \boldsymbol{\sigma}}$ and $\frac{\partial J_3}{\partial \boldsymbol{\sigma}}$ are deviatoric tensors.

$$\dot{\boldsymbol{\varepsilon}}_{pvol} = \; trace \; (\dot{\boldsymbol{\varepsilon}}_p) = \lambda \; trace \; \left(\frac{\partial Q_P}{\partial \boldsymbol{\sigma}} \right) = 3 \; \lambda \; \frac{\partial Q_P}{\partial I_1} \qquad (3.10)$$

A standard measure of inelastic deformation is the effective plastic strain rate, defined by the plastic shear components. For metal plasticity under the von Mises or Tresca criteria, the volumetric plastic strain rate $\dot{\boldsymbol{\varepsilon}}_{pvol}$ is always zero because the plastic potential is independent of the invariant $I_1(\boldsymbol{\sigma})$. This is known as J_2 plasticity. Incompressible plastic deformation is experimentally observed in metals.

3.4.2. Porous Plasticity.

The Porous Plastic subnode was also tried. This subnode for porous plastic materials was developed because modeling of plastic deformation in soils, porous metals, and aggregates has the main difference concerning traditional metal plasticity; the yield function and plastic potential are not only defined in terms of the deviatoric stress tensor (or the deviatoric stress invariant J_2), but also include dependencies on the hydrostatic pressure.

A key concept for porous plasticity models is the evolution of the relative density, which is the solid volume fraction in a porous mixture. The relative density is related to the porosity (or void volume fraction) Φ by

$$\rho_{rel} = (1 - \Phi) \qquad (3.11)$$

When compacting a mixture of metal particles or a porous material, the porosity tends to be zero, and the relative density tends to be one. There are different porous plasticity models available in COMSOL Multiphysics to account for the mechanism of compaction and void growth, among them: the Shimaâ€“Oyane Criterion [52] developed for modeling the compaction of porous metallic structures fabricated by sintering; the Gurson Criterion, the Gurson-Tvergaard-Needleman Criterion.

The Gurson criterion consists of a pressure-dependent yield function to describe the constitutive response of porous metals [26]. This yield function is derived from the analytical expression of an isolated void immersed in a continuum medium. The void volume fraction, or porosity ϕ, is the primary variable. The yield function is not an ellipse in the stress space, as in the Shima-Oyane Criterion, but it is defined in terms of the hyperbolic cosine function. The plastic potential for the Gurson criterion reads

$$Q_p(\sigma) = \left(\frac{\sigma_e}{\sigma_{ys0}}\right)^2 + 2\ \Phi\ \cosh\left(\frac{3\ p_m}{2\ \sigma_{ys0}}\right) - (1 - \Phi^2) \qquad (3.12)$$

Where σ_e is the equivalent stress (von Mises, for this study), σ_{ys0} is the initial yield stress, p_m is the pressure, and Φ is the porosity.

Tvergaard and Needleman modified The Gurson Criterion for porous plasticity to include parameters better to fit experimental data [64]. Only the unmodified Gurson Criterion was used in the current study to avoid the empirical parameters. For all the porous plasticity criteria, the change in relative density is, by default, computed from the change in plastic volumetric strain

$$\dot{\rho}_{rel} = \dot{\rho_{rel}}\ \dot{\varepsilon}_{pvol} \qquad (3.13)$$

Since the relative density is related to the porosity Φ by $\rho_{rel} = 1 - \Phi$, the change in porosity is also controlled by the change in plastic volumetric strain

$$\dot{\Phi} = (1 - \Phi)\ \dot{\varepsilon}_{pvol} \qquad (3.14)$$

and the change in volumetric plastic strain $\dot{\varepsilon}_{pvol}$ is given by the porous plasticity model.

3.4.3. POST-YIELD BEHAVIOR.

Post-yield behavior is typically characterized as being perfectly plastic (exhibits neither hardening nor softening) or showing some strain hardening, a material response in which the yield stress increases with increasing strain beyond the initial yield point Figure 3.16.

Kinematic and Isotropic Hardening models have been developed. In Kinematic Hardening, the yield surface remains constant in size and translates in the direction of yielding. Subsequent yield in compression is decreased by the amount that the yield stress in tension increased so that a difference of twice the yield

strength between the yields is constantly maintained (Bauschinger effect). Kine-
matic hardening is generally used for minor strain and cyclic loading applications.
Therefore, it was not used in the current study. Materials can be modeled as hav-
ing both Kinematic and Isotropic Hardening, called Mixed Hardening, and can be
implemented in COMSOL Multiphysics by enabling both models. However, it was
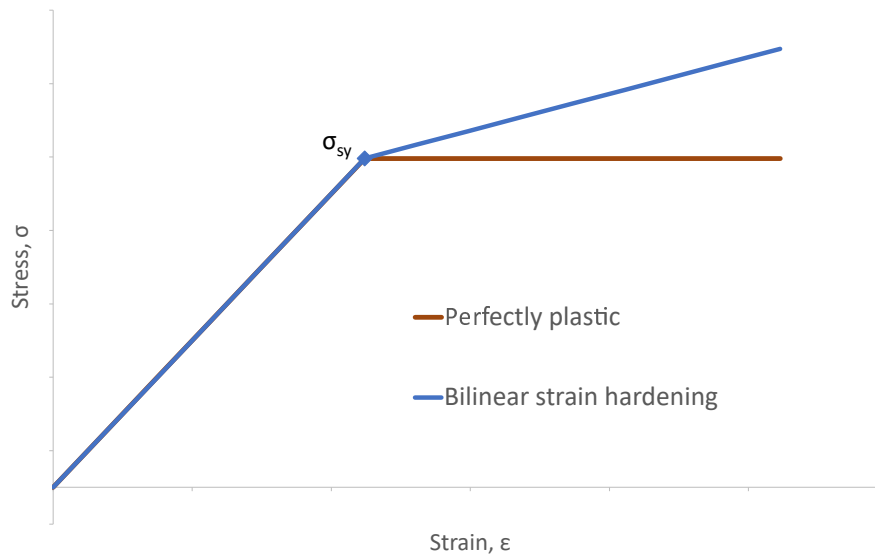not used in the current study.

Figure 3.16.: Post yield behavior, perfectly plastic and bilinear strain hardening

In Isotropic Hardening, the yield surface expands uniformly (isotropic) in all
directions with the plastic flow, and the subsequent yield in compression is equal
to the highest stress attained during the tensile phase. Isotropic hardening is often
used for considerable strain or proportional loading simulations. It is usually not
applicable for cyclic loading.

The Isotropic Hardening model can be implemented by linear (bilinear), Lud-
wik (power law), Jonhson-Cook, or hardening function, among other models. The
bilinear isotropic and the hardening function models were evaluated alongside no
strain hardening (perfectly plastic material) because they only required one or no
parameter. All other models required multiple empirical parameters, and since
there was no empirical stress-strain test for the dense material, those models were
not considered.

The Linear Isotropic hardening model implemented in COMSOL Multiphysics
is a bilinear strain hardening model. The isotropic tangent modulus E_t corresponds
to the slope of the stress-strain line after the yield point. It uses values from the
material or user-defined. The yield level σ_{ys} is modified as hardening occurs, and

it is related to the effective plastic strain ε_{pe} as

$$\boldsymbol{\sigma}_{ys} = \boldsymbol{\sigma}_{ys0} + E_{iso}\boldsymbol{\varepsilon}_{pe} \tag{3.15}$$

with

$$\frac{1}{E_{iso}} = \frac{1}{E_t} - \frac{1}{E} \tag{3.16}$$

Different values of E_t were used to mimic the experimental stress-strain behavior.

For the linear isotropic hardening model, the yield stress increases proportionally to the effective plastic strain ε_{pe}. The Young's modulus E is taken from the elastic material properties, and the hardening function $\sigma_h(\varepsilon_{pe})$ uses values from the material. The yield level σ_{ys} is modified as

$$\sigma_{ys} = \sigma_{ys0} + \sigma_h (\varepsilon_{pe}) \tag{3.17}$$

The hardening function can depend on more variables than the effective plastic strain, for example, the temperature, but that was not considered. The powder manufacturer does not provide the post-yield stress-stress behavior, and no test was performed on monolithic samples to obtain such behavior for the non-porous material.

Then the σ_h was implemented as a function of ε_{pe} (solid.epe in COMSOL), the following formulations were used:

$$\sigma_h = H \varepsilon_{pe} + (\sigma_{ysr} - \sigma_{ys0}) \left[1 - e^{-\zeta \varepsilon_{pe}}\right] \tag{3.18}$$

$$\sigma_h = H \varepsilon_{pe} + A \left[1 - e^{-\zeta \varepsilon_{pe}}\right] \tag{3.19}$$

$$\sigma_h = Constant \tag{3.20}$$

Where H: Hardening coefficient, σ_{ysr} : Residual yield stress, σ_{yso} : Initial yield stress, ζ: Saturation exponent and $A = (\sigma_{ysr} - \sigma_{ys0})$

Different combinations of these values did not improve the accuracy of the simulations. Leaving the constant σ_h as the best tool to approximate the non-linear behavior of the compressive tests. Several other post-yield behaviors are available in COMSOL Multiphysics, but they require using many empirical parameters; therefore, they were not considered.

3.4.4. Simulation setup.

Static mechanical compression tests were performed on the studied materials. For this reason, a stationary study was used for the simulations because it is recommended to compute deformations, stresses, and strains at static equilibrium suiting well to simulate the static compression tests.

Only one load step e.i. a configuration at which a solution is obtained, was used. However, a study extension called *auxiliary sweep* was used. The *auxiliary sweep* includes the *specified combinations* option, which solves several given combinations of values for each parameter in a list.

A parameter called disp was created and given the maximum value corresponding to a strain of 8% of the RVE size. This value was used for the boundary condition on the top of the RVE. The *disp* parameter was loaded into the auxiliary sweep, and *range(a,b,c)* was written under parameter value list, where *a* is the starting value, *b* is the step, and *c* is the end value.

Substeps are used to gradually apply a load and "record" points for the stress-strain diagram. The auxiliary sweep controls the number of substeps within a load step in which a solution is calculated. A substep size of 0.005 mm was successfully used to capture the stress-strain behavior with enough detail while showing no convergence issues.

The engineering strain ε was used for the uniaxial compression simulations:

$$\varepsilon \; = \frac{\Delta L}{L} = \frac{l - L}{L} \tag{3.21}$$

Where L is the original length, and l is the final length of the sample.

After the simulation results were available, the bottom face reaction force in the z-direction was calculated. A surface integration is performed over the bottom face using the COMSOL Multiphysics variable *solid.RFz* to obtain the reaction force. The transversal area of the samples could have been measured in nTopology to calculate the true stress. Instead, the face area of a cube of dense material was used. The engineering stress is calculated by:

$$\sigma_{Eng} \; = \; \frac{F_z}{A_0} \; = \; \frac{\iint solid.RFz \; dA)}{A_0} \tag{3.22}$$

Where F_z is the reaction force in the z-direction, A_0 is the original area of a solid cube and *solid.RFz* is the mentioned COMSOL Multiphysics z-direction reaction force variable.

An Intel Core vPro i7 11th generation processor with eight cores and 8 GB RAM computer was used to run the simulations.

4. Results

4.1. General results

The compression tests were performed on three samples of each of the selected relative densities. The curves were very similar. Therefore, just one of the curves was selected to represent the particular relative density and architecture. The yield strength and Young's modulus of the three samples were averaged and are reported using the standard deviation as the uncertainty of the average value. Figure 4.1 shows how the gyroid architectures have higher Young's modulus and yield strengths since their curves are above the curves of the Voronoi family. The numeric values of the modulus and yield strength are presented in Tables 4.5 and 4.7.

4.2. Gyroid Architectures

Initially, different boundary conditions were evaluated. Fixing all the degrees of freedom versus just one node (to avoid rigid body motion) and displacement in the direction perpendicular to the face (z-direction) were compared. Fixing just one node in the bottom was implemented by applying symmetry boundary conditions to the left and right faces, as explained in detail in the Methods section.

Figure 4.2 shows the stress-strain relationship for both boundary conditions compared to the experimental results. It can be seen how the use of symmetry and, therefore, a four times larger sample was more effective in predicting the material's actual behavior for a gyroid 0.1 relative density architecture. Table 4.1 shows that the fixed bottom boundary conditions, which are easily implemented, can only predict Young's modulus; instead, the more complicated-to-implement symmetry boundary conditions can predict Young's modulus and the offset yield
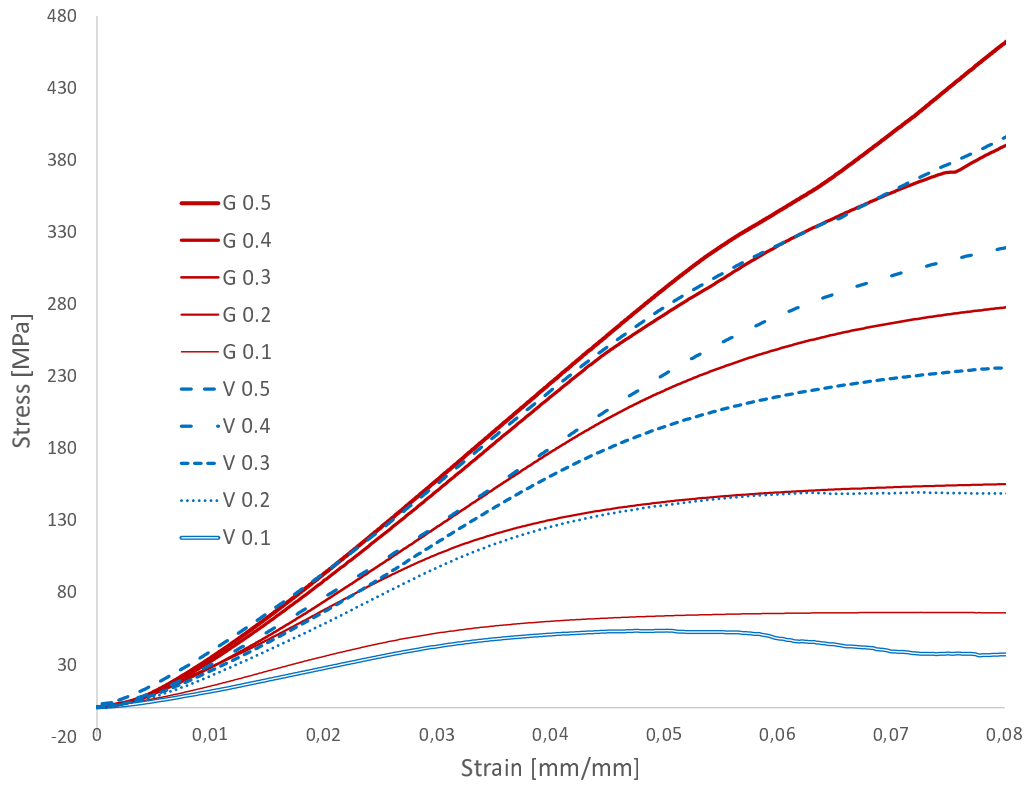
Figure 4.1.: Experimental stress-strain curves (truncated) of gyroid and Voronoi architectures. The solid red lines correspond to the gyroid architectures and the blue lines to the Voronoi [2].

strength for this architecture and relative density. Even though the experimental curve is shifted to the right, once the offset yield strength and Young's moduli are calculated, the ability of the simulation to predict both parameters becomes evident.

Table 4.1.: Effect of boundary conditions on yield strength and Young's Modulus

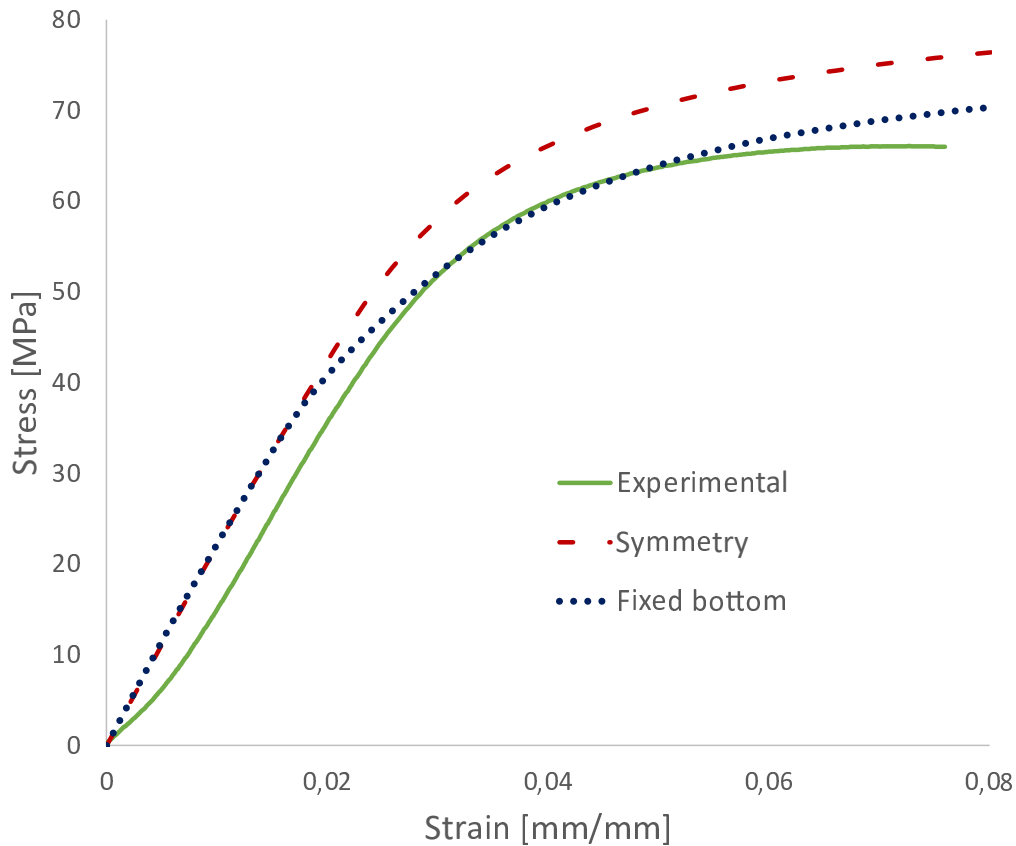| Boundary Conditions	Offset Yield Strength [MPa]	Young's Modulus [GPa]	Correlation Coefficient
Experimental Results	49.7 ± 0.16	2.02 ± 0.067	–
Symmetry Boundary Conditions	52	2.09	0.9997
Fixed Bottom	42	2.13	0.9996

Figure 4.2.: Effect of different boundary conditions in the bottom face of a unit cell of gyroid 0.1 architecture

The yield function and post-yield behavior used for the simulations from Table 4.1 and Figure 4.2 were performed using J2-plasticity and Isotropic Hardening with a constant user-defined hardening function of 1.75 GPa. The following section will describe these models' implementation in more detail. The gyroid family simulations started with the thinnest strut with a nominal thickness value of 0.2 mm and a relative density of 0.1. As seen in Figure 4.3, when the Young's Modulus of the sintered material was specified to be 126 GPa (the value reported by the powder manufacturer), the modulus of the porous material from FEA was in concordance with the experimental results.

First, no plasticity model was used; instead, a linear elastic behavior was given for the dense material, and the porous material also exhibited it. Next, the perfect plasticity model was employed. Perfectly plastic means the material can undergo plastic deformation without any increase in yield stress for subsequent load cycles. However, the yield strength was considerably lower than the experimental result.
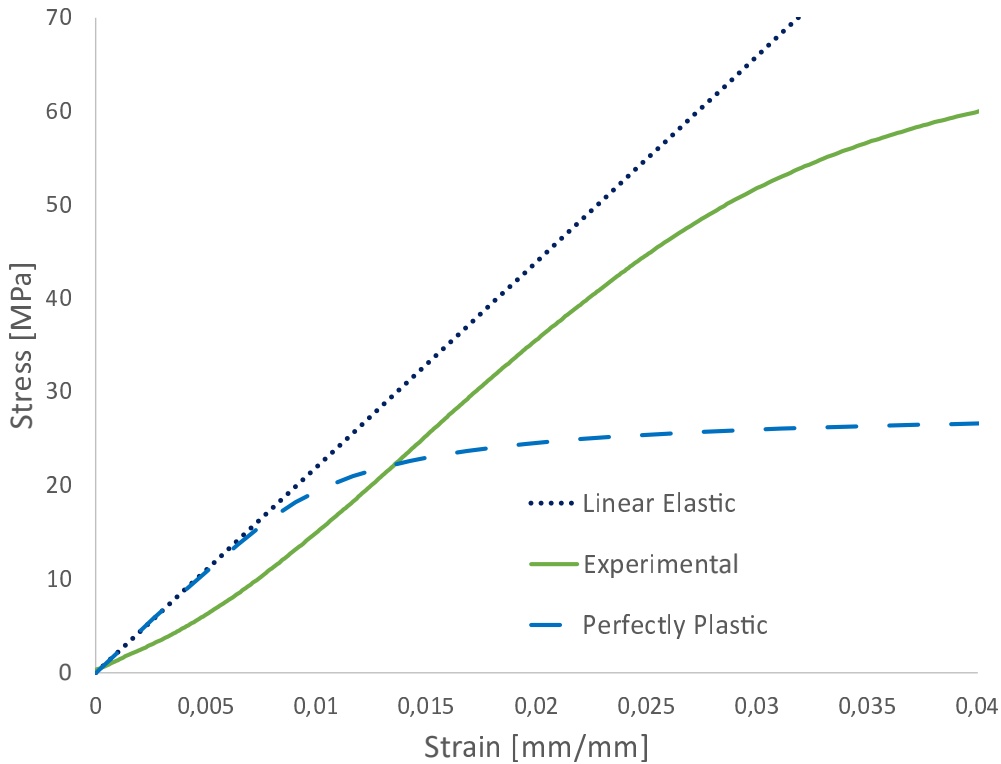
Figure 4.3.: Effect of elastic and perfectly plastic material models on stress-strain of gyroid RVE of 0.1 relative density

The Perfectly Plastic model does not account for the strain hardening in the porous material when its thin walls begin to experience localized yielding, which could explain the lower yield strength observed with that model.

The next step was to implement strain-hardening models. First, the bilinear model was tried, and Young's modulus value of E = 216 GPa was maintained while different isotropic hardening models were evaluated. Figure 24 shows that the linear isotropic hardening with an isotropic tangent modulus $E_t = 1$ GPa showed similar results to the perfectly plastic models. It takes high values of the tangent modulus, e.g., E_t= 50 GPa, for the behavior to resemble experimental values. However, the shape of the curve is not replied correctly. Moreover, the offset yield strength is about half of the experimental for all cases. Young's modulus is not affected by the post-yield behavior and continues to coincide with the slope of the experimental results.

The Hardening Function plasticity model was then tried. The best performance occurs when the isotropic hardening model's hardening function has a constant value of $\sigma_h = 1.75$ GPa, the modulus, offset yield strength, and non-linear
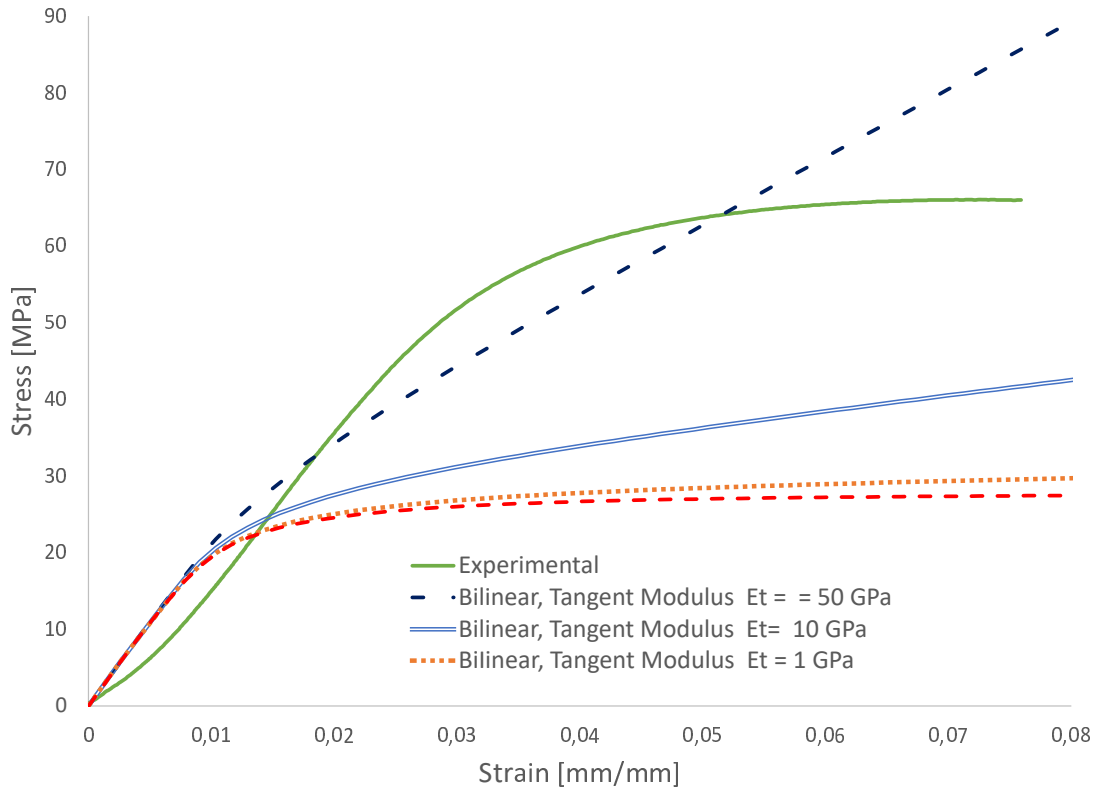
Figure 4.4.: Stress-strain for bilinear plasticity model with different Tangent moduli E_t evaluated with $E = 126$ GPa for Gyroid structure of 0.1 relative density

post behavior are close to the experimental results. Figure 4.5 shows the effect of considering an exponential function, a linear term, or a constant.

Figure 4.6 shows the equivalent von Mises stress plot for simulating the gyroid architecture of 0.1 relative density. Plastic behavior is expected since the stress values are above 887 MPa, which was used as the yield value for the solid titanium alloy. The stresses are considerably higher once the strain hardening model is activated, compared with the perfect plastic where no strain hardening occurs.

The von Misses stresses in the volume plot are considerably higher than the stresses in the stress-strain diagrams due to the use of the complete area of the cube as if it were solid to calculate the stress-strain plots of the porous materials. The stress distribution in both cases is not uniform.

The Porous Plasticity node was introduced, substituting the Plasticity node. It requires the definition of a void volume fraction or porosity, which is not to be confused with the porosity of the architected material. The void volume frac-
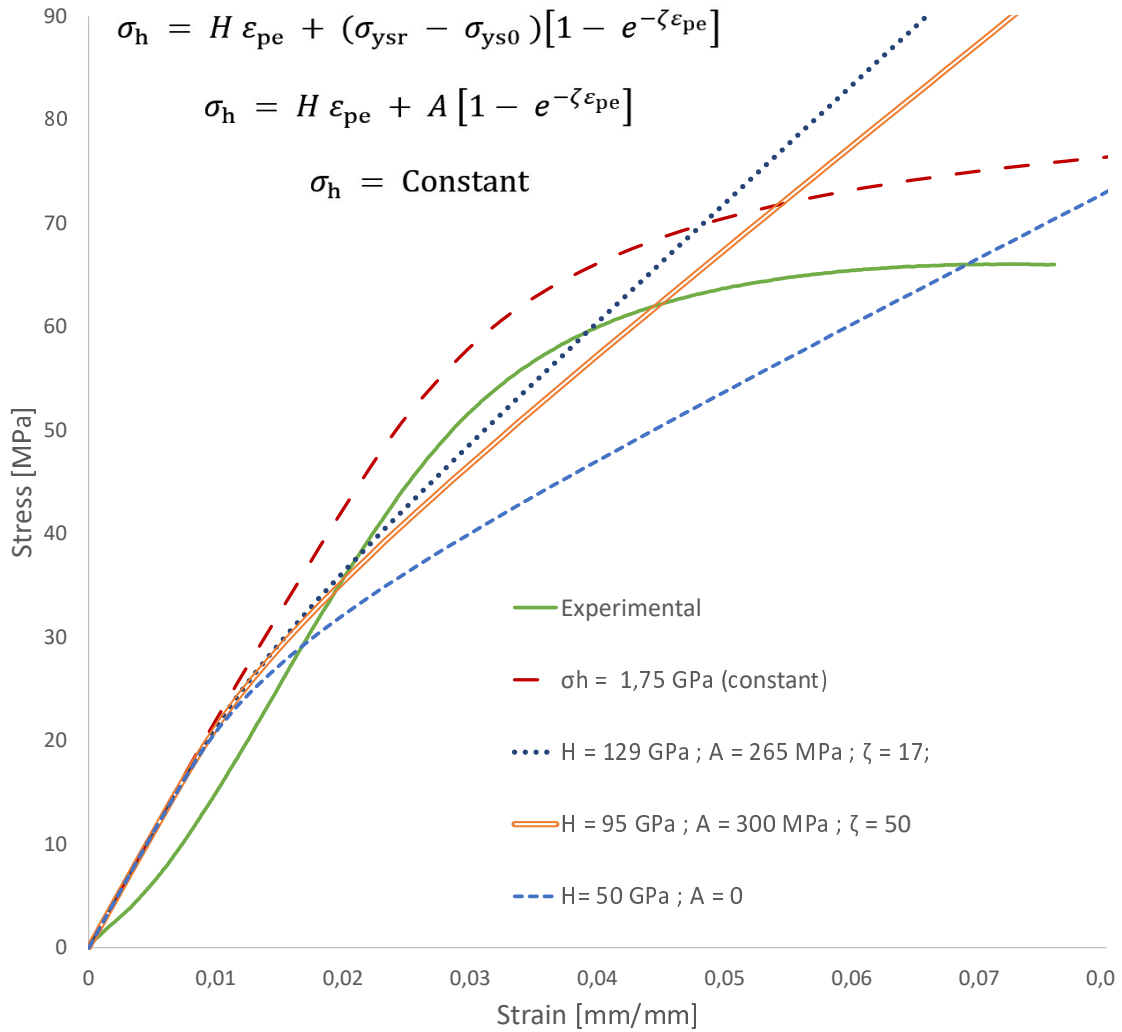
Figure 4.5.: Stress-strain for Hardening Function plasticity model evaluated with E = 126 GPa for gyroid structure of 0.1 relative density and different parameters

tion represents voids in the additively manufactured walls of the gyroid structure. Therefore, values around 10% void volume fractions were used. In Porous Plasticity, the yield criterion is no longer von Mises. Instead, the Gurson yield function, which incorporates the void volume fraction, is used.

Concerning the post-yield behavior, the same models from the Plasticity node are available in Porous Plasticity (Isotropic Hardening, Kinematic Hardening, Mixed Hardening). The Isotropic Hardening with a constant hardening function

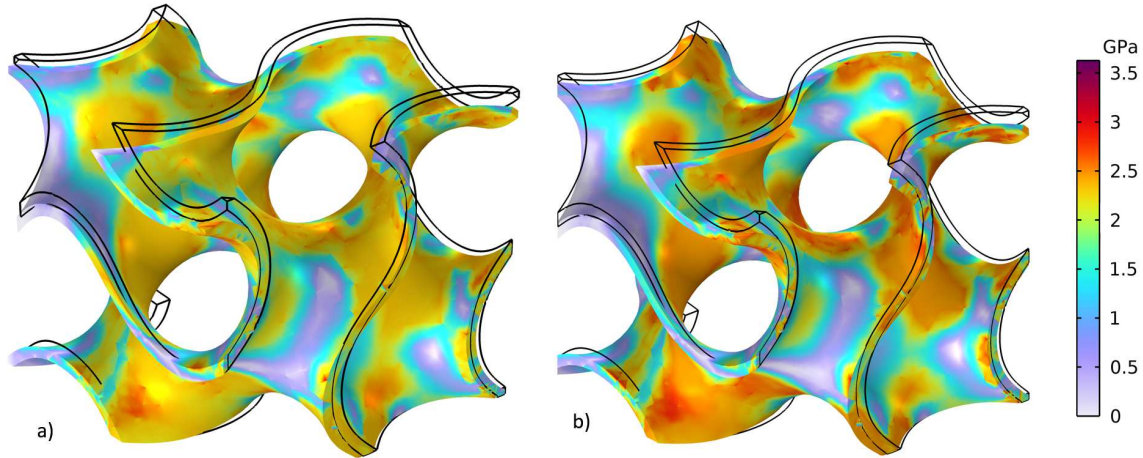**Figure 4.6.:** Von Misses Stress plot for gyroid architecture a) perfectly plastic b) strain hardening with constant hardening function.

was also employed. Figure 4.7shows how the yield strength decreases with increasing void volume fractionâsuggesting that an internal porosity between 0.05 and 0.1 might be found in the struts of this gyroid architecture.

The 0.002 offset yield strength, obtained graphically from Figure 4.7, is presented in Table 6. The yield strength of the porous plasticity model with a volume of 0.05 coincides with the experimental result.

Table 4.2.: Offset yield strength and Young's modulus for different plasticity models and void volumes of 0.1 relative density gyroid architecture

Plasticity Model	Offset Yield Strength [MPa]	Young's Modulus [GPa]	Correlation Coefficient
Experimental	49.7 ± 0.16	2.02 ± 0.067	
Plasticity	52	2.09	0.9996
Porous Plasticity, f0 = 0.05	50	2.09	0.9996
Porous Plasticity, f0 = 0.1	48	2.09	0.9996

The stress-strain curves for different plasticity models and parameters of the gyroid architecture of 0.2 relative density are shown in Figure 4.8. The Plasticity curve corresponds to the isotropic strain hardening with the 1.75 GPa constant strain hardening function and E = 126 MPa. Then porous plasticity is introduced with the same parameters and void volume fractions of 0.05 and 0.1. The Young's
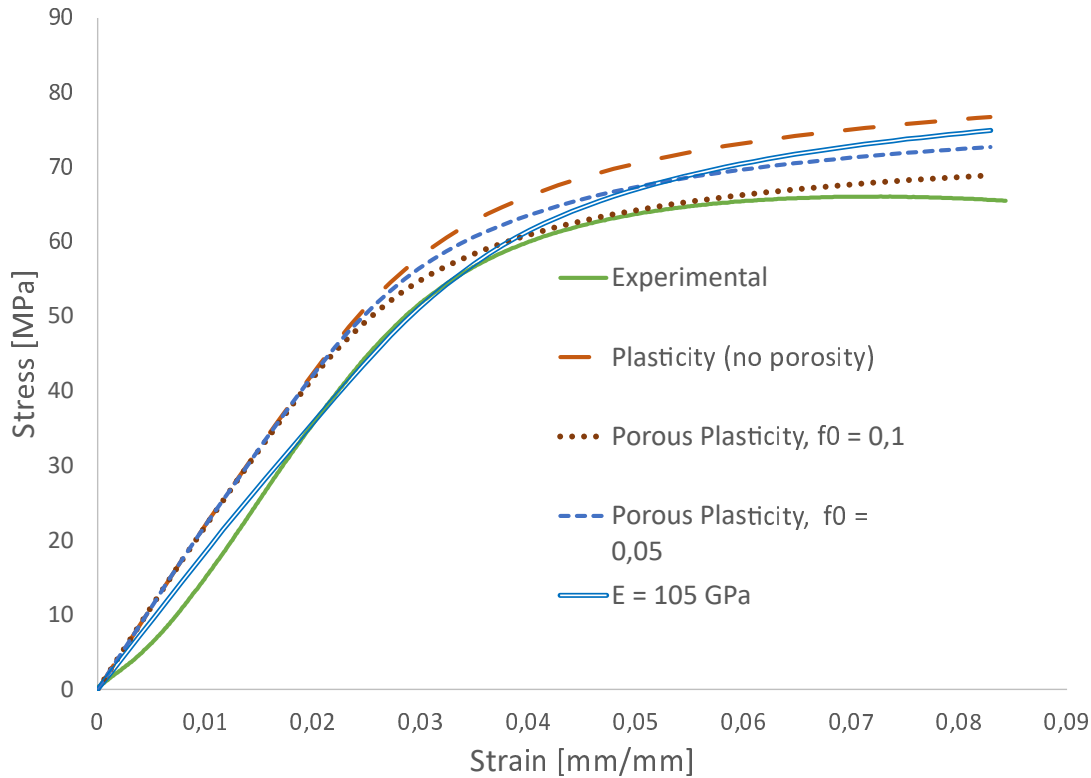
Figure 4.7.: Stress-strain with porous plasticity for different values of void volumes, compared to experimental and regular plasticity for gyroid material of 0.1 relative density.

modulus of the gyroid material obtained from the simulations does not match the experimental's. Only when the dense material's E is lowered to 80 MPa, the simulation matches the experimental Young's modulus for the porous material.

The gyroid architecture of 0.3 relative density was first simulated with the plasticity node, and the constant hardening function developed for the 0.1 density. Figure 4.9 shows the general mechanical behavior from the experiment and the simulations, and Table 4.3 the offset yield strengths and Young's Moduli obtained from the stress-strain plot.

The simulation with the plasticity node predicts the offset yield strength with an error of 14%, which improves with the porous plasticity node. The best result for the yield strength is found with a void volume fraction of 0.1, where the yield strength is only 3%. The von Misses stress distribution from Figure 4.9 shows how the stress is more or less evenly distributed among the walls of the gyroid structure.
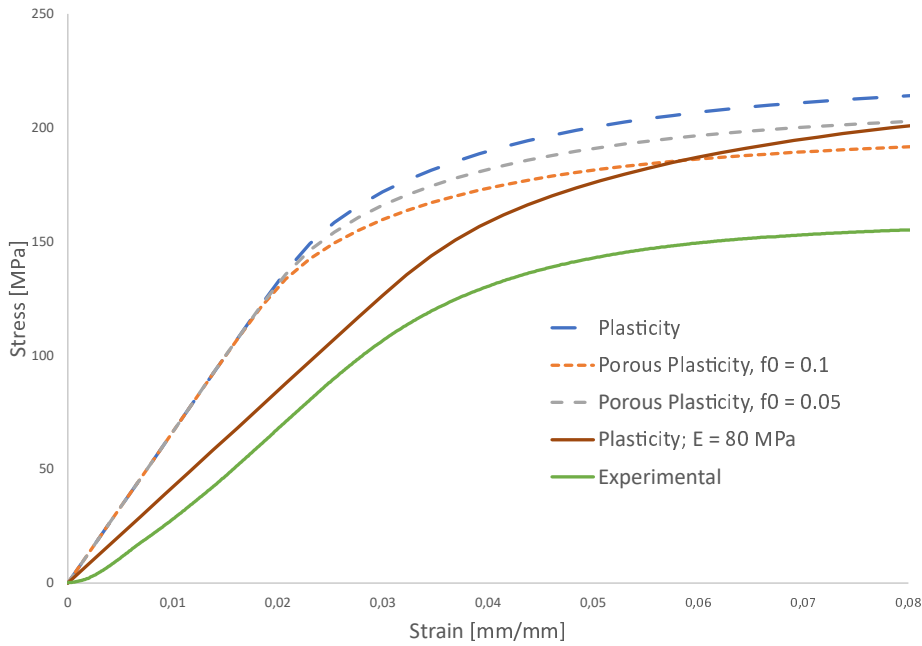
Figure 4.8.: Stress-strain behavior of gyroid 0.2 relative density with different void volume fractions and Young's modulus.

The effectivity of the simulation to predict Young's modulus is diminished compared to the 0.1 density. It is necessary to lower the dense material's modulus to 62 GPa to match the experimental modulus. Nevertheless, with this lower modulus, the simulation offset yield strength remains only 1% off the experimental's.

Figure 28.

The strain-stress results for the gyroid architecture of 0.4 relative density are shown in Figure 4.10. Similar to the previous cases, the simulation with plasticity and isotropic strain hardening can predict the yield strength of the material (see Table 4.5). This prediction improves with the use of porous plasticity. However, regarding the Young's modulus, it is necessary to assign a value of E = 45 MPa for the dense material in order for the simulation to match the Young's modulus of the compression test.

As seen in Table **??**, the ability of the porous plasticity node to predict the offset yield strength diminishes for the 0.5 relative density gyroid architecture. The regular plasticity with the constant hardening function provides the best results for this architecture. Figure 4.11 shows the behavior of the stress-strain relationship and Table **??**.

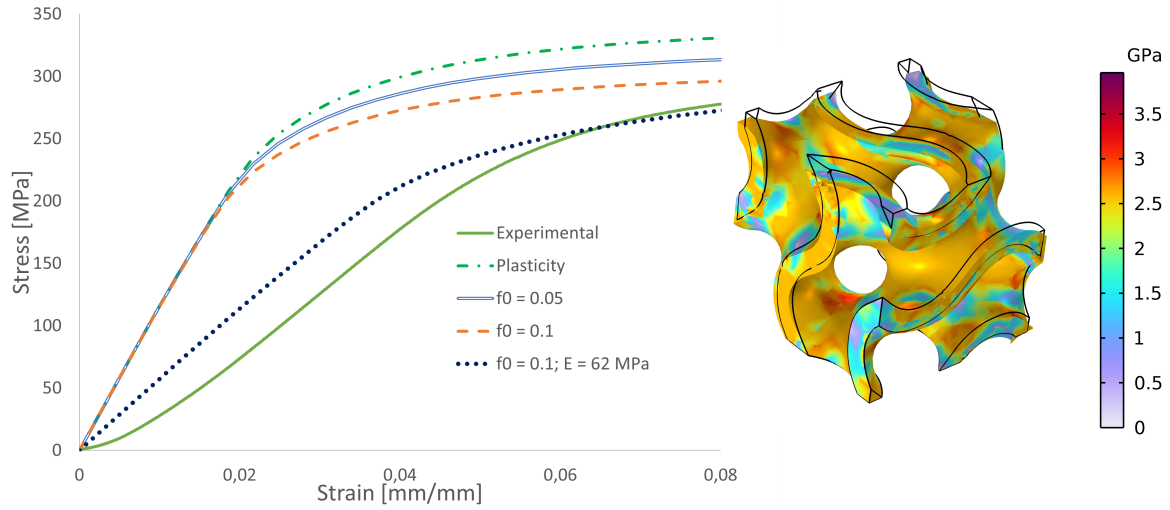The difference between the simulated and experimental modulus increased

Figure 4.9.: Stress-strain behavior of gyroid 0.3 relative density with different void volume fractions and Young's modulus. On the right side, the von Misses stresses for a sample of the same relative density.

Table 4.3.: Offset yield strength for different plasticity models and void volumes of 0.3 relative density gyroid architecture

Plasticity Model	Offset Yield Strength [MPa]	Simulation error [%]	Young's Modulus [GPa]	Correlation Coefficient	Simulation error [%]
Experimental	222 ± 3.4	–	5.3 ± 0.07	0.9998	–
Plasticity	248	12	11.18	0.9997	111
PP, f0 = 0.05	237	7	11.18	0.9997	111
PP, f0 = 0.1	224	1	11.18	0.9997	111
PP, f0 = 0.1 E=55 GPa	217	-2	5.05	0.9999	-5

*PP: Porous plasticity

vastly for this relative density. As shown in It is necessary to lower the modulus of the dense Titanium alloy to 30 GPa in order for the simulation to have the same slope (modulus) as the compression test results.

Table 4.5 summarizes the results of the offset yield strength and Young's modulus for the gyroid family. The simulations were performed using the same plasticity node, strain hardening model (isotropic hardening, constant hardening function), and Young's modulus for the laser-sintered powder (126 GPa). The simulations can predict the yield strength, but only the 0.1 relative density simulations have an acceptable accuracy concerning the experimental Young's Modulus.
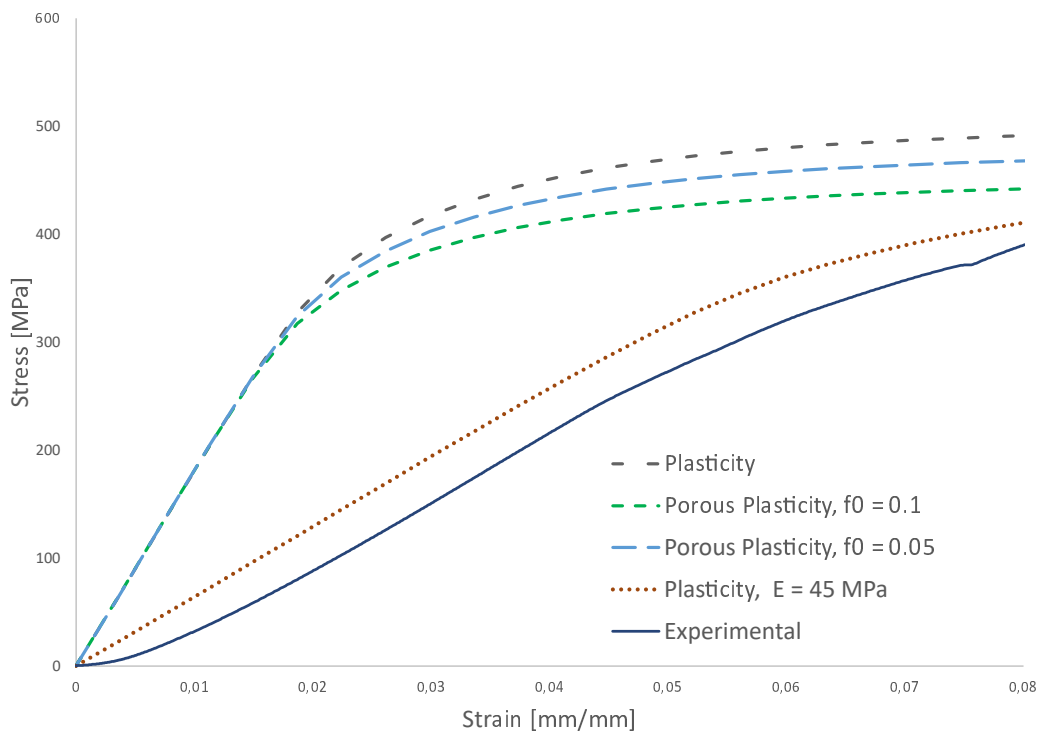
Figure 4.10.: Stress-strain behavior of gyroid 0.4 relative density with different void volume fractions and Young's modulus.
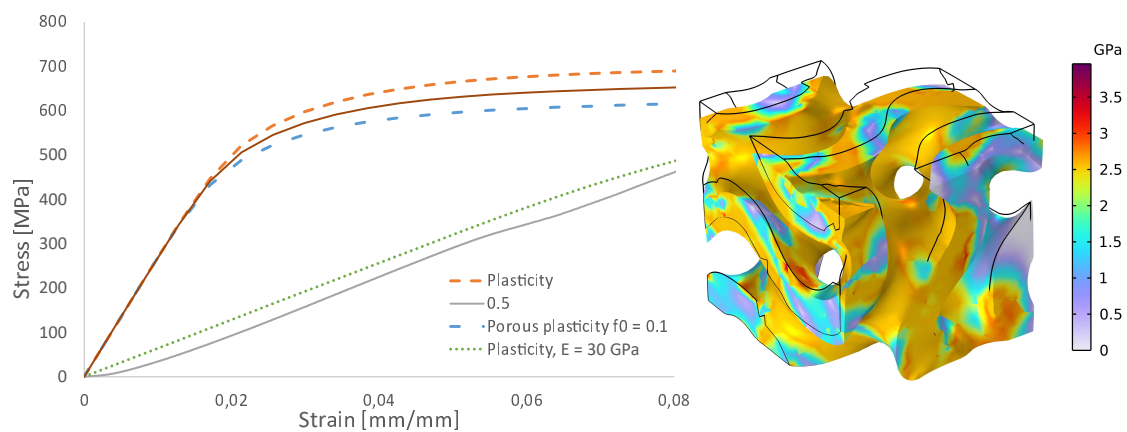

Figure 4.11.: Stress-strain behavior of gyroid 0.5 relative density with different void volume fractions and Young's modulus. On the right side, the von Misses stresses for a sample of the same relative density.

Table 4.4.: Offset yield strength and Young's modulus for different plasticity models and void volumes of 0.5 relative density gyroid architecture

Plasticity Model	Offset Yield Strength [MPa]	Simulation error [%]	Young's Modulus [GPa]	Correlation Coefficient	Simulation error [%]
Experimental	494 ± 2.9	–	6.47 ± 0.003	–	–
Plasticity	520	5	26.19	0.9997	305
PP, f0 = 0.1	460	-7	26.19	0.9997	305
PP, f0 = 0.05	486	-2	26.19	0.9997	305
P, E = 30 GPa	460	-7	6.32	0.9999	-2

*PP: Porous plasticity
*P: Plasticity

Table 4.5.: Offset yield strength and Young's modulus for different relative densities of gyroid architecture

Relative Density	Offset Yield Strength [MPa]		Simulation error [%]	Young's Modulus [GPa]		Simulation error [%]
	experiment	simulation		experiment	simulation	
0.1	49.7 ± 0.16	52	5%	2.02 ± 0.067	2.09	4%
0.2	118 ± 4	160	36%	4.1 ± 0.02	6.467	58%
0.3	222 ± 3.4	248	12%	5.3 ± 0.07	11.18	111%
0.4	336 ± 7	370	10%	6.1 ± 0.01	17.54	188%
0.5	494 ± 2.9	520	5%	6.47 ± 0.003	26.19	305%

Figure 4.12shows the offset yield strength for different relative densities. The experimental results are compared with the plasticity (isotropic hardening, constant hardening function) and the porous plasticity with the same hardening function but different void volume fractions.

The 0.05 void volume fraction is most accurate for the 0.5 and 0.4 relative densities. The 0.1 void volume produces the most accurate yield strength results for all other densities. In all cases, porous plasticity has more accuracy than just plasticity.

Figure 4.13shows Young's modulus for each relative density predicted by the simulations and the experimental results. The inability of the simulations to predict Young's moduli becomes evident as soon as the relative density is higher than 0.1.

An interesting result can be obtained if the Young's modulus of the dense material required to match the slope of the linear elastic section of the stress-strain curve experimental result is plotted for each relative density (Figure 4.14). An
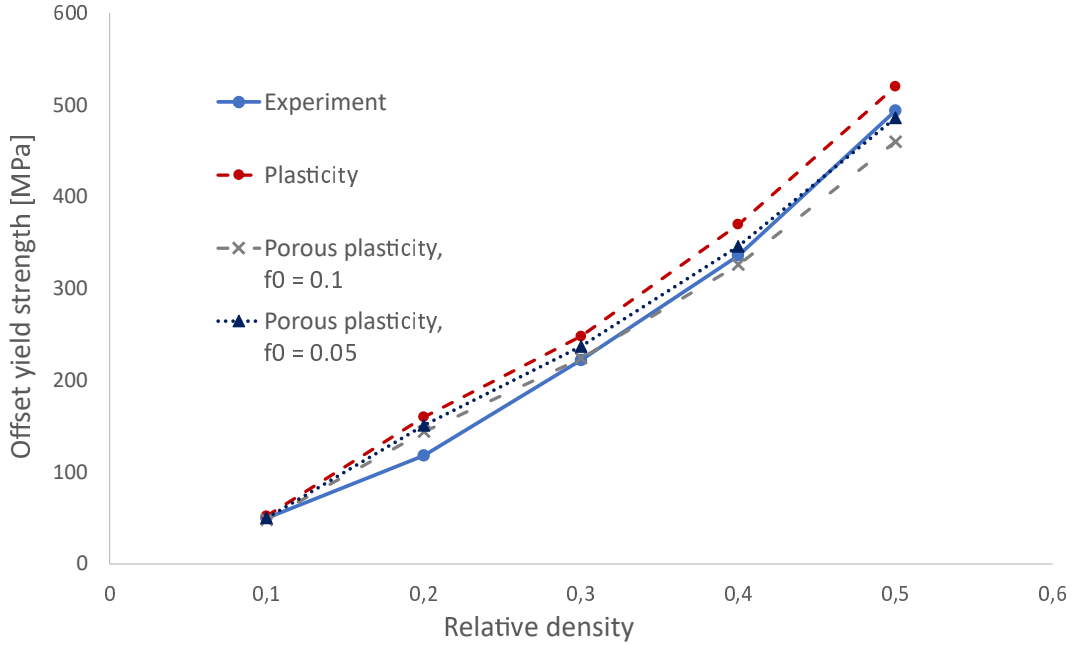
Figure 4.12.: Comparison between simulations with different plasticity models and void volumes and experimental results for offset yield strength for all the gyroid densities

aproximated linear relation is found, starting with the 126 GPa reported by the manufacturer for a unitary relative density (solid material without porosity) and skipping the 0.1 relative density, whose E was effectively matched by the simulations. This could be used as an empirical rule for future simulations until more accurate models are developed. The following equation represents that approximated linear relationship:

$$E_{Dense\ modified} = (E_{Dense} - 166,7 * \rho_{rel}) \quad [GPa] \quad (4.1)$$

Where $E_{Dense\ modified}$ is the new Young's modulus that must be used for the simulation so that the results match the experimental results. E_{Dense} is the original Young's modulus as reported by the powder manufacturer and ρ_{rel} is the relative density of interest.

4.3. VORONOI ARCHITECTURES

The different boundary conditions were evaluated for a cube of 2 mm. Table 4.5 shows how using artificial plates combined with symmetry boundary conditions
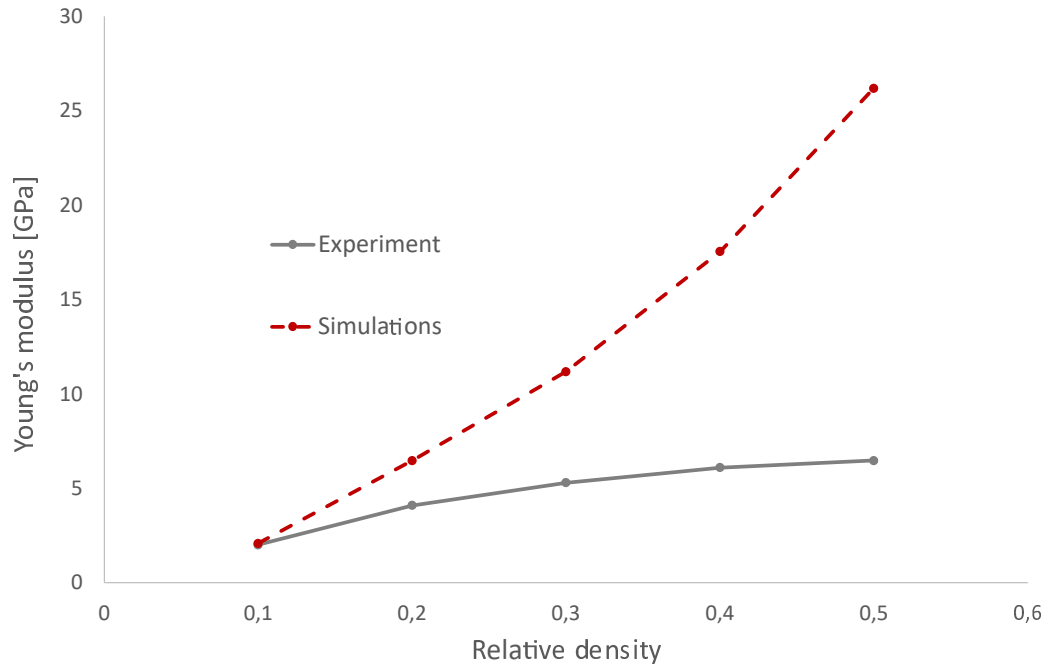
Figure 4.13.: Young's modulus comparison between simulation and experimental results for different relative densities of gyroid architecture.

produces the most accurate results. This result is similar to what was verified for the gyroid geometries. The Young's modulus and yield strength used for the simulation were 126 GPa and 887 MPa, respectively.

The isotropic hardening plasticity model with a constant hardening function of 1.75 GPa investigated with the gyroid family was also employed.

Unlike what occurred with the gyroid geometries, to evaluate different boundary conditions, it was necessary to modify the geometry of the RVE. Figure 34 shows how this geometry modification affected the stress-strain results of the simulations. The use of the plane faces as a boundary condition, as shown in Figure 4.15 b), implied that some struts were sliced and became very thin, which might explain the very low modulus and strength for that case. The Voronoi material simulation with the appropriate boundary conditions, likewise the gyroid of 0.1 relative density, can predict the experimental Young's modulus. However, the prediction of the yield strength is not as accurate as it was for the gyroid of the same relative density.

Once the best boundary conditions were found, the influence of the RVE size was investigated. The 0.1 relative density of the Voronoi showed unusual behavior. As seen in Figure 4.16, the closest to the observed behavior was obtained with the
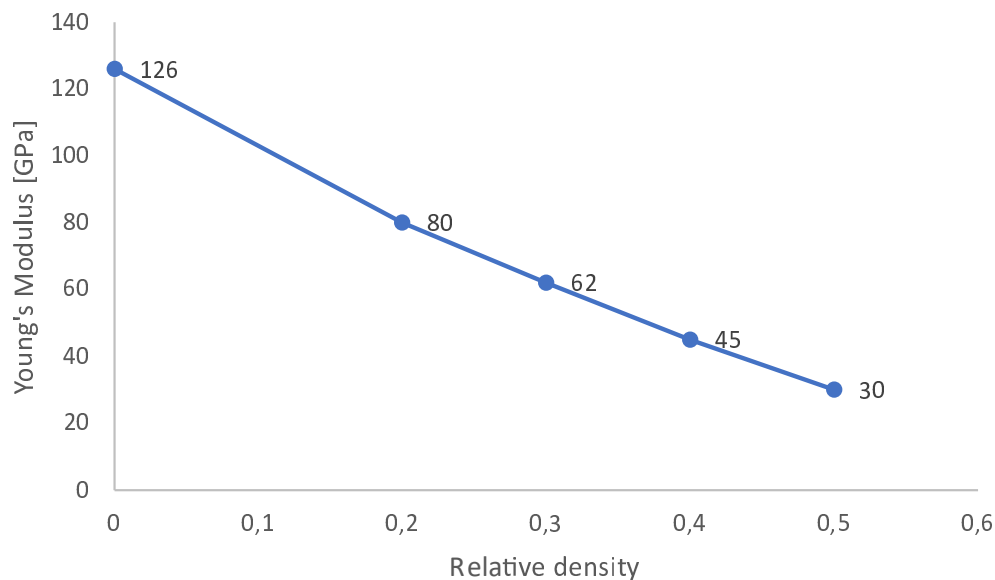
Figure 4.14.: Modified Young's modulus of dense material to match the simulation and experimental Young's modulus of the porous gyroid architectures.

Table 4.6.: Offset yield strength and Young's modulus for different boundary conditions of 0.1 relative density Voronoi architecture

Boundary Conditions	Offset Yield Strength [MPa]	Young's Modulus [GPa]	Correlation Coefficient
Experimental Results	46 ± 0.5	1.5 ± 0.12	–
Artificial plates (symmetry)	31.6	1.3	0.9998
Struts Only	21.6	0.78	0.9996
Plane faces	9.2	0.31	0.9997

smallest RVE of 2 mm.

Figure 4.17 b) and c) show some lateral unstressed struts. These lateral struts in the 3 and 4 mm RVE sizes are not vertically connected to the top and bottom structures. Therefore, they do not carry any vertical load, which other struts in the center of the RVE must support. On the contrary, Figure 4.17 a) shows how all the struts are vertically connected to the top and bottom plates and bear the stress, which might explain its more accurate results.
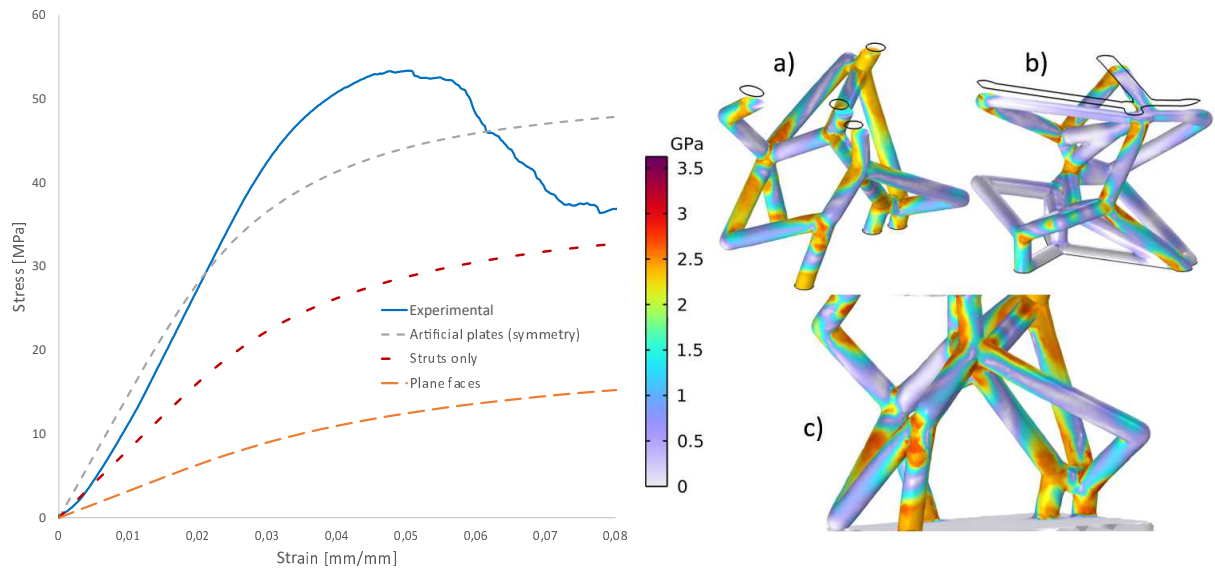
Figure 4.15.: The stress-strain plot of different boundary conditions implemented for Voronoi architecture of 0.1 relative density and von Mises stress plots for a) only struts, b) plane faces, and c) artificial plates with symmetry

The Voronoi architectures are stochastically generated. Therefore, different structures can be produced with the same RVE size, strut diameter, and relative density, which behave differently in the simulations. It is believed that these stochastic effects might be averaged for large enough samples. Unfortunately, it was not possible to simulate larger samples because the meshing algorithms in COMSOL encountered problems with effectively meshing larger than 4 mm RVEs of these architectures, especially for higher relative densities.

A study was performed with the 0.5 relative density to analyze the effect of different stochastic configurations of the same relative density. Figure 4.18 shows the stress-strain plot for different configurations of the same relative density, strut, and RVE size. It also shows the von Mises stress plot for the 1.2 mm RVE. The 1.2 mm RVE is unsuitable because its reduced size oversimplifies the architecture. The Young's modulus of the oversimplified 1.2 mm size RVE is similar to the experimental result. However, the yield strength is deficient.

The presence of semi-horizontally oriented struts not connected to the top and bottom plates can be verified in versions v1 and v3 (see Figure 4.19). These struts are mostly unstressed, causing the other to bear most of the load, producing a lower yield strength of the whole structure.
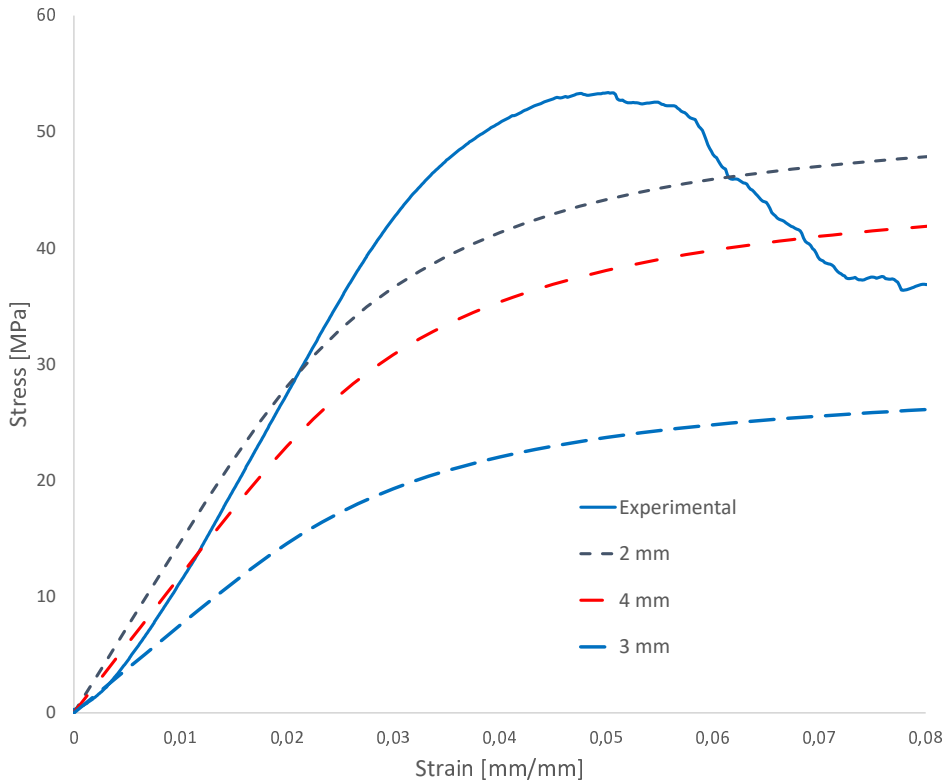
Figure 4.16.: Stress-strain plot for cubes of 2, 3, and 4 mm of Voronoi architecture of 0.1 relative density.

On the contrary, in versions v2 and v4 (especially in v2), most struts bear axial loading. Consequently, their stress-strain curves show a stiffer behavior and a higher yield strength. Version v2 has a yield strength of 432 MPa, comparable to the 389 ± 6.2 from the mechanical tests; its Young's modulus is 19.3 GPa, while the experimental value is 5.4 ± 0.05 GPa for a difference of 257%, not far from the 305% difference between the modulus of the simulations and the experimental results for the gyroid family.

For version v2 of the 1.8 mm RVE, the porous plasticity node was applied with a void volume fraction of 0.1, bringing the yield strength results to only 1% below the experimental result.

The empirical rule developed for the gyroid architectures, which consisted in decreasing E of the dense material according to a linear progression, was employed for the optimal version of the 1.8 mm cube. According to that empirical rule, a Young's modulus of 30 GPa was selected for the dense material. The stress-strain curve obtained from the simulation for the porous Voronoi architecture of
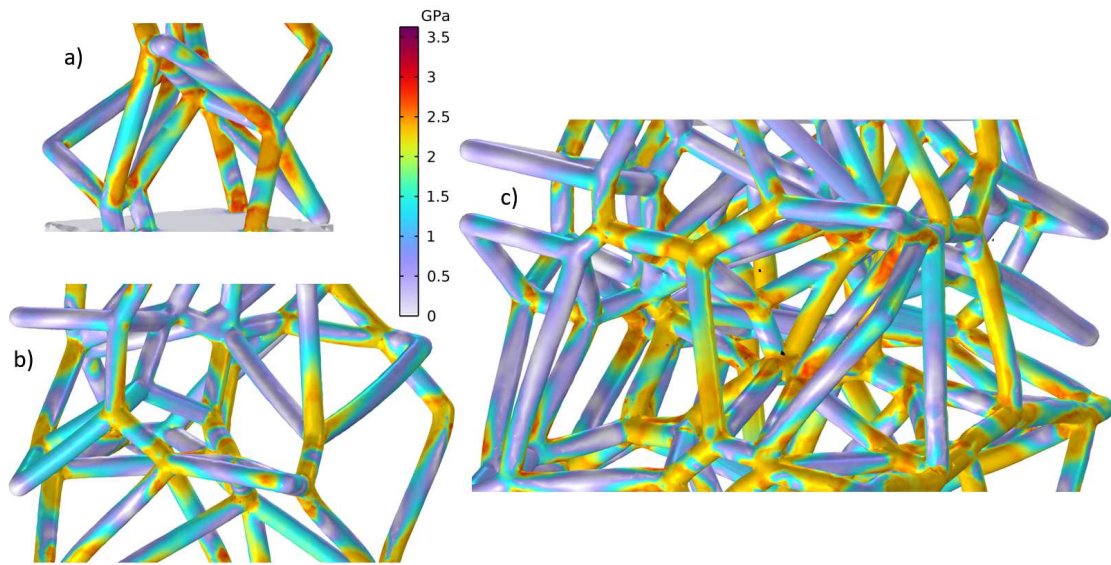
Figure 4.17.: Von Mises stress plots for a) 2, b) 3, and c) 4 mm cubes of architecture of 0.1 relative density.
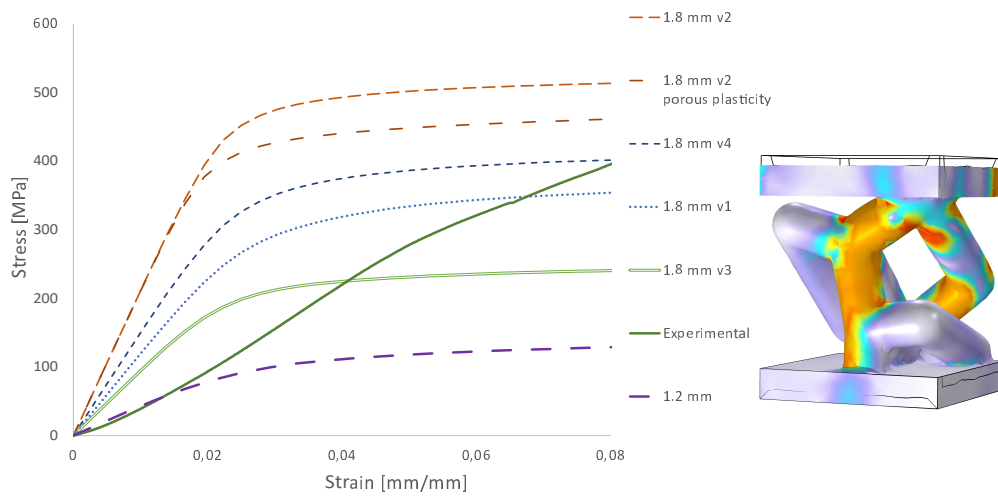
Figure 4.18.: The stress-strain plot of Voronoi architecture of 0.5 relative density. Different stochastic configurations for the 1.8 mm RVE size and one configuration for the 1.2 mm RVE size. On the right side, von Mises stress of the 1.2 mm RVE.

0.5 relative density has a slope of the linear section corresponding to 5.03 GPa, only a 6.8% percent off from the 5.4 GPa experimental result.
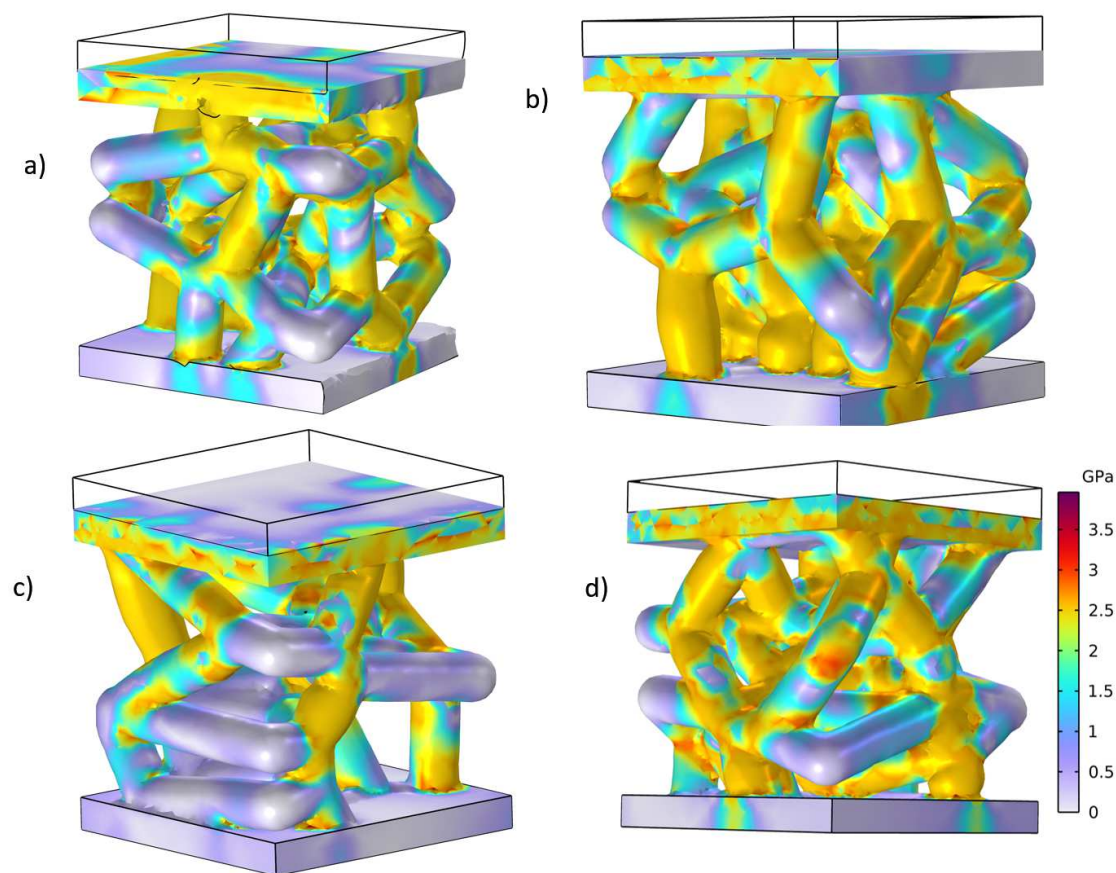
Figure 4.19.: Von Misses stresses for different configurations of Voronoi architecture for an RVE size of 1.8 mm. a) v1, b) v2, c) v3, and d) v4

Figure 4.20 shows how for the 0.2 relative density, the sizes of 1.5 and 2mm RVEs seem too small to capture the material's constitutive behavior. The 3 mm size with 84 MPa yield strength comes closer to the 121 ± 1.4 MPa of the experiments. The optimal RVE size is more extensive but close to 3 mm for this relative density. The Young's modulus is the same as the experimental for the 3mm RVE size. However, the information obtained from the gyroid family and the Voronoi cube of 1.8 mm shows that this match is just a coincidence.

Figure 4.20 also shows the effect of removing all degrees of freedom from the bottom face (fixed bottom). It can be compared with the same 3 mm RVE but different boundary conditions: only removing the degree of freedom of displacement parallel to the compression test direction. Using the fixed bottom boundary conditions, as consistently occurred during this study, causes the yield strength to be lower and farther from the experimental results. Fixed boundary conditions

have an advantage, though they are computationally more efficient. For example, the 3 mm RVE took 34 minutes and 26 seconds to complete with the symmetry boundary conditions versus 23 minutes and 32 seconds with the fixed bottom making them 32% more computationally effective.

Figure 4.20.: Stress-strain plot for Voronoi architecture of 0.2 relative density. On the right side, von Mises stress plot for a) 1.5, b) 2, and c) 3 mm RVE size.

Figure 4.21 shows a very similar situation occurs for the Voronoi architecture of 0.3 relative density. The 1.2 mm cube is too small to correctly represent the material's behavior because its yield strength is too low. The 2 mm RVE modulus is close to the experimental, but it is considered coincidental given the behavior of the gyroid models. The optimal RVE size must be larger than 2 mm because the yield strength of the 2 mm cube is still low.

Figure 4.22 shows the stress-strain plot of the 0.4 relative density for cube sizes 1.1 and 2 mm, which are very similar. The yield strength is below the experimental by 33%, and the modulus is 53% above the experimental result. The von Mises stress plots show the stress distribution in the structures. Both have most struts bearing the axial compressive load, which explains their similar results.

Table 11 shows the yield strength and modulus obtained using the best RVE for each relative density. In most cases, that was the largest RVE possible to simulate with the current method. The exception corresponds to the 0.1 relative
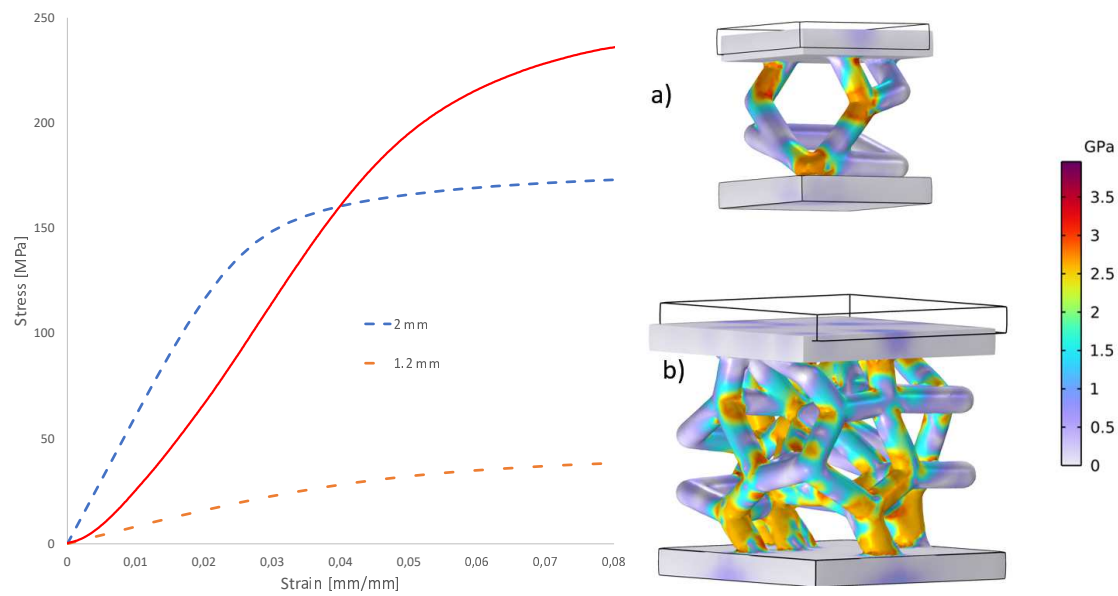
Figure 4.21.: Stress-strain plot for Voronoi architecture of 0.3 relative density. On the right side, von Mises stress plot for a) 1.2 and b) 2 mm RVE size.

density where 4 mm RVES were simulated; however, the 2 mm RVE results are considered better after analyzing the stress distribution in the struts.

Table 11, Figure 4.23, and Figure 4.24 show that the ability of the simulations to predict the yield strength of the Voronoi materials for the RVE sizes considered is not as good as it was for the gyroid materials. The error percentage is still low enough to provide a general idea of the material's behavior from the simulations. Figure 42 only includes one point for the porous plasticity. It was only evaluated for the 1.8 mm cube size of the 0.5 relative density.
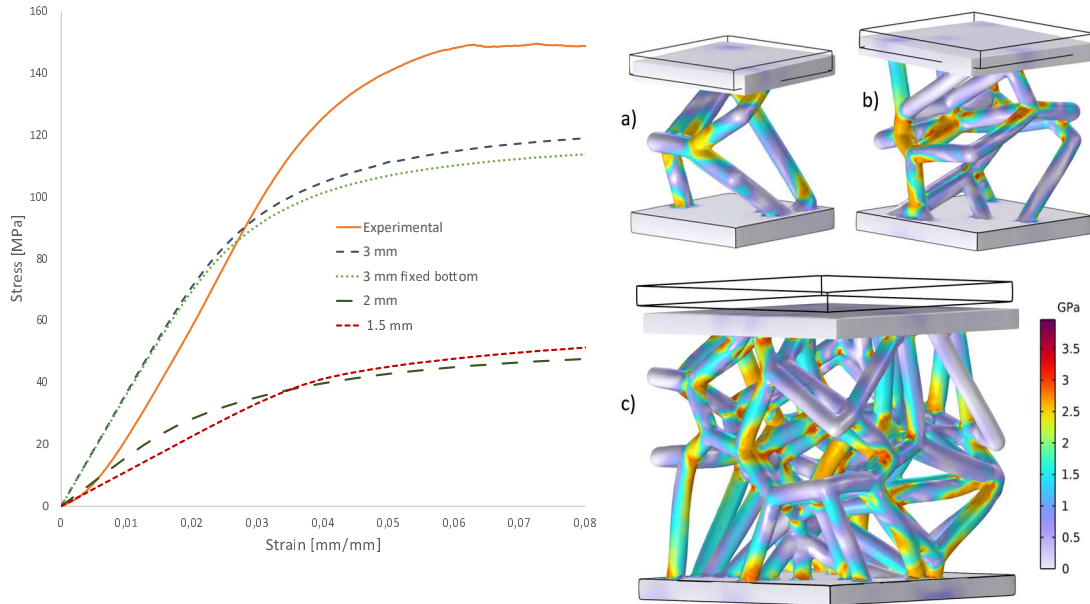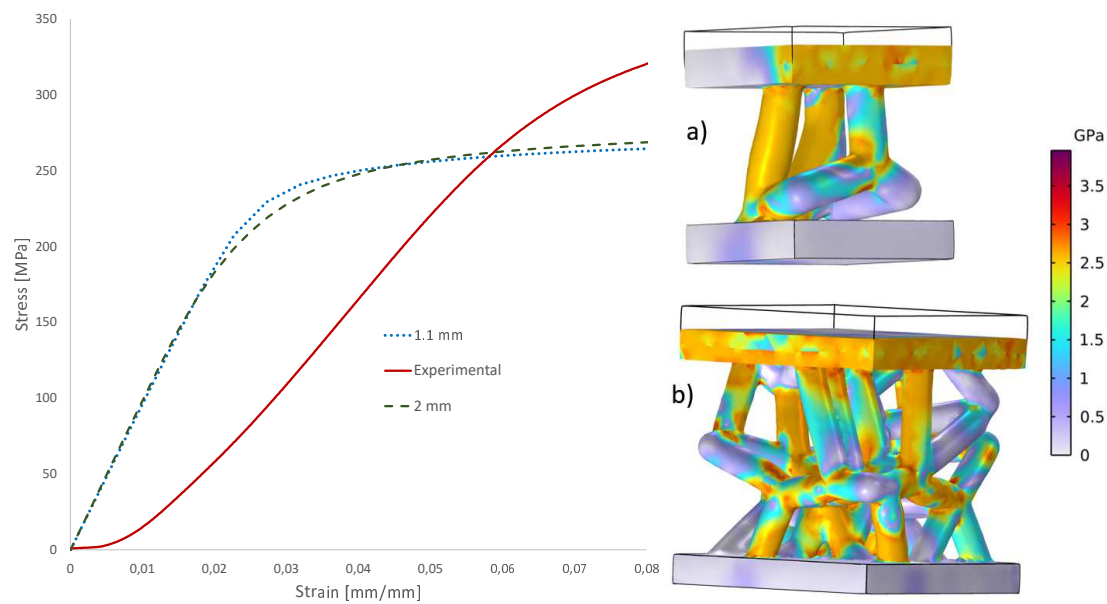
Figure 4.22.: Stress-strain plot for Voronoi architecture of 0.4 relative density. On the right side, von Mises stress plot for a) 1.1, b) 2, and c) 3 mm RVE size.

Table 4.7.: Offset yield strength and Young's modulus for different relative densities of Voronoi architecture.

Plasticity Model	Offset Yield Strength [MPa]	Simulation error [%]	Young's Modulus [GPa]	Correlation Coefficient	Simulation error [%]
Experimental	494 ± 2.9	–	6.47 ± 0.003	–	–
Plasticity	520	5	26.19	0.9997	305
PP, f0 = 0.1	460	-7	26.19	0.9997	305
PP, f0 = 0.05	486	-2	26.19	0.9997	305
P, E = 30 GPa	460	-7	6.32	0.9999	-2

*PP: Porous plasticity
*P: Plasticity

Figure 4.23.: Comparison between simulations with different plasticity models and void volumes and experimental results for offset yield strength.
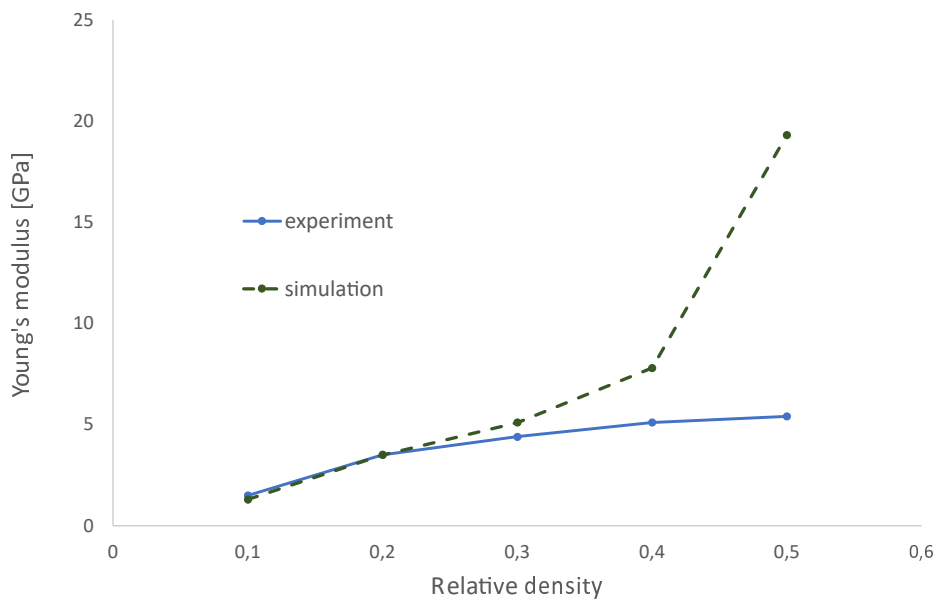
Figure 4.24.: Young's modulus comparison between simulation and experimental results for different relative densities of Voronoi architecture.

5. DISCUSSION

5.1. REFERENCE TO THE AIM OF THE STUDY

The FEA simulations of the periodic gyroid architectures were performed following a comprehensive path starting from selecting the most suitable boundary conditions. It was found that the use of symmetry boundary conditions and only one fixed point located at the center of the model (to avoid rigid body motion), only restricting the bottom face's degree of freedom parallel to the compression test direction, was the most effective to replicate the experimental stress-strain curves with the simulations.

The use of an elastoplasticity material model and an isotropic strain hardening model with a constant strain hardening function of 1.75 GPa was found essential for the simulated mech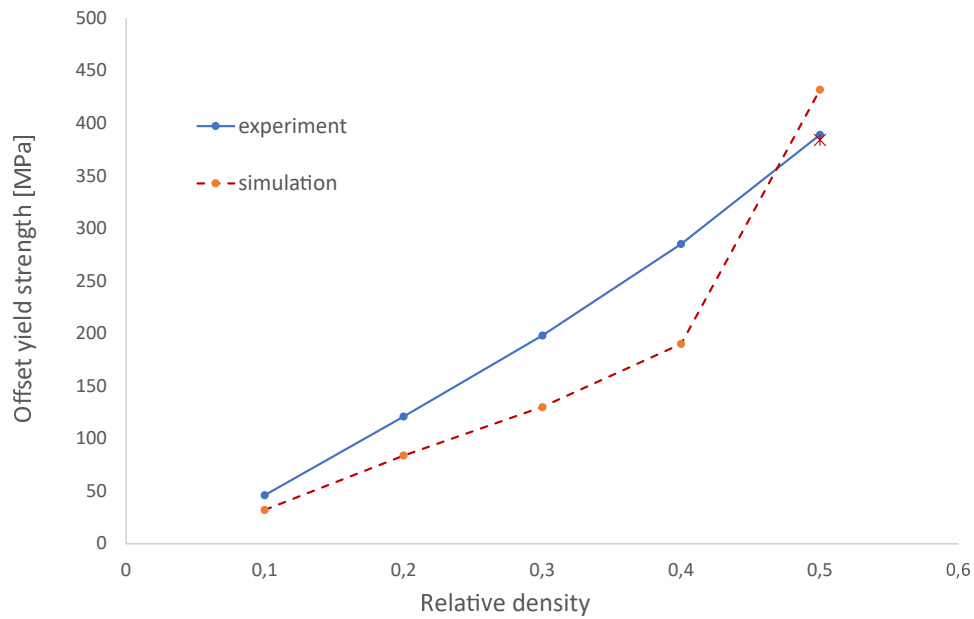anical behavior in compression to resemble the experimental's. The simulations effectively predicted the materials' yield strength for all the ranges of relative densities from 0.1 to 0.5 of the gyroid architectures. Using the Gurson criterion (a plastic porosity model) with a void volume between 0.05 and 0.1 increased the accuracy of the yield strength prediction. The use of this porosity model to account for the internal porosity of the walls and struts of the porous architectures improving the accuracy of the yield strength prediction was not previously reported in the literature.

The ability of the simulations of the gyroid architectures using the unitary cell as RVE to predict the Young's modulus was only practical for low relative densities (below 0.2). Changes in the plasticity model or the strain-hardening model did not affect the simulations' Young's modulus. Only by changing the material's parameters from the 126 GPa reported by the powder manufacturer was it possible to match the experimental Young's modulus with the results of the FEA simulations.

The parameters and models that offered the best results for the gyroid materials were used to study the optimal RVE size for the Voronoi family. Increasing the RVE size was generally found to improve the ability of the simulations to predict the yield strength. The Young's moduli of the Voronoi family predicted by the simulations were more accurate than for the gyroid family. However, prudence is recommended with these results until larger Voronoi RVEs of these materials are simulated.

The Voronoi tesselation has a stochastical nature. Random points in space create each Voronoi cell. Different location for the initial points means different material structures, even though the same relative densities and strut diameters are used. The effect of those differences in the microstructure likely fades away for large enough material samples, but for the sizes considered in the simulations of the present study, the effect was significant. Therefore, not only the RVE size was to be considered for the Voronoi simulations but an adequate stress distribution over all the struts. Some of the RVEs generated had struts that were not directly connected vertically with the rest of the structure. Von Mises stress plots of those RVEs show those struts were under very low stress. The other struts from the RVE were bearing most of the stress. Therefore, the effective area was reduced, causing lower yield strength values for the simulations to be much lower than the experimental results.

The only case in which the present study can affirm the size of an RVE for the Voronoi architecture in the whole meaning of the name, e.i., represents the material's macroscopic behavior concerning the yield strength, was the cube of 1.8 mm side length for the 0.5 relative density. Native mesh generation errors made it impossible to simulate larger RVEs than those reported for the densities between 0.1 and 0.4. However, it is believed that the adequate RVE size for those relative densities of Voronoi architectures is not far from the largest cubes simulated in the present study.

5.2. REVIEW OF IMPORTANT FINDINGS

The employment of a plasticity model was fundamental for the simulations to accurately predict the yield strength of both gyroid and Voronoi architectures. Figure 4.3 shows how using a perfectly plastic model for the models, where the material experiences no hardening or softening, produces a nonlinear stress-strain behavior, which is convenient but insufficient to obtain accurate yield strength values. Bilinear isotropic hardening models were implemented, and while increasing values of the tangent modulus were more effective in mimicking the stress-strain curve shape, their yield strength values were too low compared with the experi-

mental (Figure 4.4). After some experimentation with strain hardening functions, it was found that a constant strain hardening function of 1.75 GPa effectively predicted the stress-strain curve shape and the experimental yield strength (Figure 4.5).

Pores are a common defect of SLM, and they were found in the experimental compression samples. A Gurson porous plasticity model was implemented in COMSOL Multiphysics, and porosities ranging from 0.05 and 0.1 of void volume fraction improved the accuracy of the prediction of the yield strength of the gyroid architectures for all of the relative densities of the gyroid family evaluated (Figure 4.12) and also for the only Voronoi element whose RVE size is considered to have been found. The fact that the porous plasticity can considerably improve the accuracy of the yield strength predictions suggests that the SLM additively manufactured materials considered in this study might have an internal porosity of around 10%.

All experimental stress-strain plots present a section of nonlinear fast deformation under a low load. Subsequently, the stress-strain curve presents the characteristic linear elastic behavior until the yield point is reached. This initial nonlinear section might be related to some initial yielding of struts or parts of the architecture with manufacturing errors diminishing their stress-bearing capabilities. Once these weak structures collapse, the architecture's linear elastic behavior occurs. The plot's linear section slope corresponds to the experimental Young's modulus.

The Young's modulus was predicted accurately only for low relative densities (0.1 and 0.2). Afterward, it diverges from the experimental results, a trend reported in the literature. Changing the plasticity models and parameters did not affect the simulated Young's modulus. Only modifications on the Young modulus of the dense material effectively lower the porous architectures' modulus to match the experimental's.

The increasing divergence between the modulus from simulations and experiments with increasing relative density might be related to the manufacturing process. It was found that the surface roughness and porosity increase with growing relative density. This might imply that the manufacturing process might weaken the material of the thicker struts and walls. As more material must be sintered, more heat has to be introduced, and the heat dissipation might also be impaired, possibly causing slower cooling rates which are known to lower the stiffness of this type of material.

Nevertheless, the empirical rule developed to predict the Young's modulus of new architectures was satisfactorily employed to predict the modulus of the Voronoi material of 0.5 relative density.

5.3. Limitations and justifications

The main limitation corresponds to the COMSOL Multiphysics native mesh generation for the FEA. The geometries generated in nTopology must be transformed into volumetric meshes to be importable in COMSOL. Joining operations must be carried out in the imported mesh part to remove artificial edges where struts intersect. In some cases, this operation was sufficient to create a functional solid adequately processed by COMSOL's meshing algorithm. The meshing operation failed on other occasions, especially for larger RVE volumes and densities. Modifying the importing parameters, refining the mesh size, performing Fill Holes operation on the mesh, and adding and removing elements proved insufficient to obtain a working FEA mesh.

It was necessary to generate an entirely new model in nTopology, with the same relative density and strut diameter, until the stochastic parameters created a geometry that could be successfully imported into COMSOL Multiphysics. The more intricate the geometry, which occurs with increasing relative density, the more likely problems occur. The possibility of randomly generated small holes in the structure increased with increasing RVE size. Therefore, obtaining a working model for sizes larger than 3 mm was difficult.

Figure 5.1 shows an example of a small hole caused by the Voronoi tesselation's stochastic nature. COMSOL Multiphysics meshing algorithm had problems incorporating these tiny holes, causing Self-intersection errors. Many attempts were made to remove them from the imported nTopology, and refine the mesh. However, the most effective way found was to generate a whole new model in nTopology. An iterative and time-consuming trial-and-error process had to be implemented to obtain fully functional models.

It is possible to use imported meshes in COMSOL Multiphysics without creating a solid and a new native mesh from that solid. However, it could not be implemented because the nTopology mesh is a void crust, just the external surface representation, which is not feasible for 3D structural simulations.

Young's Moduli are calculated from the linear sections of the curves. The correlation coefficients are used to determine if the data used for the Young's moduli correspond with a linear relation. The values from Table 5 are very close to one, which means the assumption of linear behavior for the data considered to calculate Young's Moduli is valid.

Mesh convergence studies were performed across the study. However, the mesh refinement only duplicated the computing times without significantly impacting the mechanical properties.
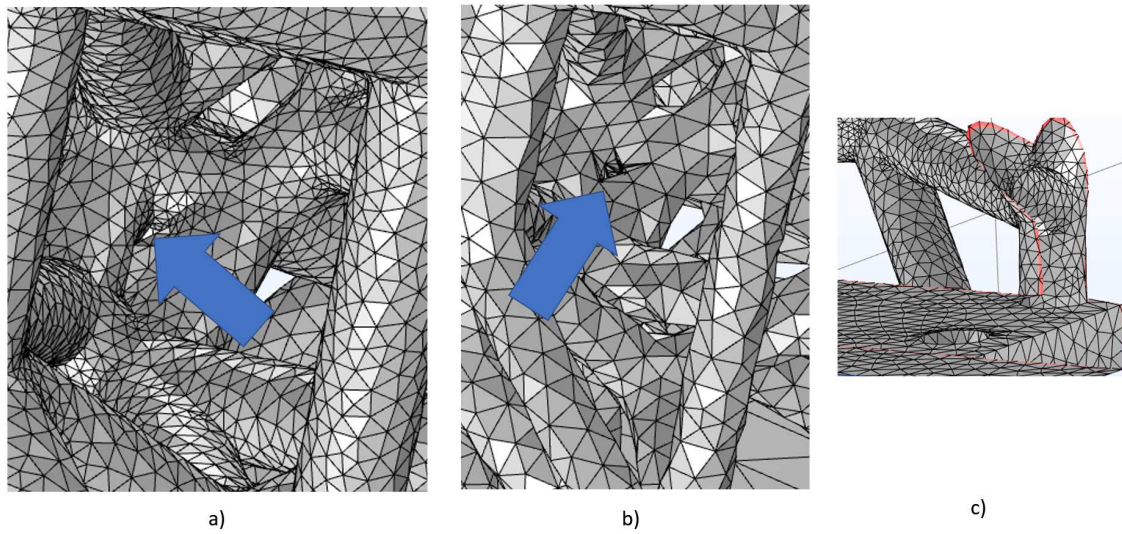
Figure 5.1.: Imported Voronoi of 0.5 relative density mesh after a) joining process and b) after meshing in COMSOL, c) shows a section view of imported mesh.

The powder manufacturer reported the properties for solid materials, not porous ones like those manufactured. Manufacturing deviations related to the manufacturing parameters or the fact that a porous instead of a solid structure was manufactured can cause the walls and struts of the porous material to have internal micro-pores or superficial adherences of unmelted material.

Additionally, the input heat from the laser and the differences in cooling rates can affect the microstructure and create manufacturing stresses. The heat treatment after the fabrication was performed following the manufacturer's indications, but it could have been a source of deviation from the properties reported by the manufacturer for a solid MDLS sintered material.

Computational homogenization is available in COMSOL Multiphysics. However, it was not viable to utilize the cell periodicity node on the RVEs of this study. The Voronoi architecture could not be included due to its lack of symmetry between the opposing faces of the RVE. The gyroid unit cells are symmetric; however, it was impossible to create a symmetric mesh for opposing sides due to the curved nature of the geometry. The homogenized material model, which can be incorporated into a user-defined material model, was not achieved.

5.4. Comparisons between different elements of the present study

In addition to the comparisons already performed, it is essential to discuss the computation times. The processing time increased with the relative density. Gyroid RVEs of 0.1 relative density took around one minute, while the relative density of 0.5 took 2 minutes. The 4 mm cubes of Voronoi relative density 0.1 took 30 minutes to solve, while the 1.8 mm RVE of 0.5 relative density took 5 minutes to solve. Implementing the porous plasticity model increased the computational effort while bringing increased accuracy to predict the yield strength.

The von Mises stress plots across this study show how the stress is more evenly distributed over the entire volume of the triply periodic minimal gyroid surfaces. At the same time, in the case of the Voronoi architectures, there are several stress concentrators at the intersection between struts, and in general, the stress distribution is far less uniform. These stress concentration areas might explain the experimental's lower yield strengths of the Voronoi materials.

5.5. Comparisons with previous works

The use of boundary conditions where all degrees of freedom are eliminated for the bottom face of the samples or RVEs is used by [76], [21], [40], [56], [65] and [73]. The influence of this selection on the final results is not mentioned at all. The current study found that the fixed bottom boundary conditions consistently produced simulation results with lower yield strength than removing only the degree of freedom parallel to the compression test direction. Although widespread in the literature and easy to implement, the fixed bottom boundary conditions produced less accurate yield strength results. The fixed bottom boundary conditions did not affect Young's modulus results (see Figure 4.2 and Figure 4.20). Therefore future studies focusing on elasticity instead of yield strength might take advantage of these easily implemented fixed bottom boundary conditions. The fixed bottom boundary conditions were around 32% more computationally efficient.

The use of rigid plates with frictionless contact is implemented [3]. However, they do not explain which alternative boundary conditions were examined or support their selection. Even though the current study did not use rigid plates to compress the materials sample, the employed boundary conditions, which allow displacement of the sample in radial directions perpendicular to the axial compression direction, end up being very similar to the frictionless contact between rigid plates. The contact formulation implementation is generally more computationally expensive than the solution implemented in the current study.

[43] uses very similar boundary conditions to those implemented in the current study, only for a 2D model. A comparison against different boundary conditions is not performed. However, they note how using a displacement condition allows easy control of the calculation steps and is very useful for gaining stress-strain information. The same displacement condition for the top face (instead of applying a force or pressure) was employed in the current study with satisfactory results.

The use of bilinear isotropic hardening models is widespread in the literature [3], [27], [43]; some researchers use even the perfectly plastic model to predict the yield strength of reticular additively manufactured materials effectively. However, when implemented in this study, both produced too low values for the yield strength (Figure 3.16). Another approach found in the literature often is the use of post-yield experimental data [21], [73], [57]. Unfortunately, such data was not available for this study. It is recommended to have such data for future research, especially from tests directly performed on samples the size of the struts, attempting to incorporate the manufacturing influence for the different strut diameters or wall thicknesses.

Regarding the yield strength and Young's modulus [76]performed a similar study comparing RVE simulations with compression test results for diamond lattice DSLM additively manufactured Ti6Al4V structures. They also accurately predicted the yield strength but presented the same increasing divergence between FEA obtained and experimental Young's modulus for relative densities between 0.2 and 0.4 relative densities while using unit cells to perform the simulations. Significant discrepancies between simulation and experiments were found [21], [73]. The discrepancies may be related to the deviations between the modeled and fabricated structures [5]. Some authors can accurately predict yield strength and Young's modulus [3], but instead of a unit cell, they simulated the full-size compression sample and used relative densities between 0.1 and 0.3. Their study shows the advantage of modeling the scaffolds directly as CAD solids, which facilitates the meshing. Unfortunately, this approach is unsuitable for the gyroid and Voronoi structures considered in the present study. Besides, it is possible that the additive manufacturing of their models with flat faces involves fewer problems than manufacturing the geometries of this study.

Stacking several unit cells for simulation has been found to lower the FEA-obtained Young's modulus by 4.5 GPa when four unit cells were stacked together [40]. However, this is impractical for the current study, first because of the difficulties importing and meshing larger samples from nTopology, and, secondly, because the discrepancies found in this study are considerably higher than 4.5 GPa.

5.6. Implications and generalizations

A general procedure to create simulations of gyroid and Voronoi or similar architected materials can be reconstructed from the current study. It is recommended to start from the lowest relative densities and with periodic materials. Experimentation should be performed to determine the best boundary conditions, plasticity models, strain hardening models, and their parameters best suiting for the lowest relative densities and periodic materials. Then the information obtained can be used to model the more complex stochastic non-periodic structures and higher relative densities. The effectivity of the developed empirical rule to predict the Young's modulus of porous materials can be tried for different material architectures.

5.7. Recommendations for future research

Exploring new methods in COMSOL Multiphysics to import and mesh larger sample sizes from nTopology remains challenging for future research. Also, cuasi-meshless simulation methods look promising to simulate this kind of architecture, avoiding the described problems with native FEA mesh generation.

Even though compression is the primary load mode considered for bone replacement materials, the simulation of other load modes like torsion and fatigue possess high research potential to design and optimize additively manufacturable materials, which could improve the acceptability and durability of bone implants and scaffolds.

Comprehensive studies where SLM is used to manufacture compression samples with the same size as the struts evaluated in the study might allow the use of experimentally obtained stress-strain curves for each strut diameterâincorporating that information into the post-yield behavior model of the simulations. Metallographic and microscopic analysis of the struts' internal microstructure, porosity, and presence of unmelted inclusions or adherences might help further understand the divergence of Young's modulus between simulations and experiments.

6. Conclusions

FEA simulated triple periodic minimal gyroid architecture unit cells accurately predicted the yield strength of compression samples of relative densities between 0.1 and 0.5. Using an isotropic strain hardening constant function with a value of 1.75 GPa proved better than bilinear isotropic to mimic the stress-strain behavior. Implementing a porous plasticity Gurson model with void volume fractions between 0.05 and 0.1 to account for the internal porosities in the additively manufactured walls of the gyroid material improved the accuracy of the yield strength predictions. The prediction of the Young's modulus diverged from the experimental results, a common finding in the literature. However, an empirical rule was found to predict the Young's modulus of the porous material by linearly decreasing the Young's modulus of the dense constituent material.

Increasing the size of the simulation samples of the non-periodic stochastic Voronoi materials was found to positively impact the simulations' ability to predict the compression samples' yield strength. However, guaranteeing a uniform stress distribution among the entire geometry was also essential to obtain meaningful results. A sufficiently large cube size to be considered an RVE in the whole meaning of the name was only achieved for the 0.5 relative density, with a size of 1.8 mm. The empirical rule developed for the gyroid architectures was instrumental in predicting the Young's modulus of this RVE of Voronoi architecture. Meshing errors avoided the simulation of larger cube sizes for the other relative densities of this family, as well as performing a computational homogenization for the gyroid materials.

BIBLIOGRAPHY

[1] J. Aboudi, S. M. Arnold, and B. A. Bednarcyk. *Micromechanics of composite materials: a generalized multiscale analysis approach.* Butterworth-Heinemann, 2013.

[2] M. Araya-Calvo. Development of system for biomechanical preclinical testing of customized implants on synthetic bone. *Doctoral Research Project*, 2022.

[3] A. Arjunan, M. Demetriou, A. Baroutaji, and C. Wang. Mechanical performance of highly permeable laser melted ti6al4v bone scaffolds. *Journal of the Mechanical Behavior of Biomedical Materials*, 102:103517, 2020.

[4] A. Ataee, Y. Li, D. Fraser, G. Song, and C. Wen. Anisotropic ti-6al-4v gyroid scaffolds manufactured by electron beam melting (ebm) for bone implant applications. *Materials Design*, 137:345–354, 2018.

[5] Z. S. Bagheri, D. Melancon, L. Liu, R. B. Johnston, and D. Pasini. Compensation strategy to reduce geometry and mechanics mismatches in porous biomaterials built with selective laser melting. *Journal of the Mechanical Behavior of Biomedical Materials*, 70:17–27, 2017. Mechanics of additively manufactured biomaterials and implants.

[6] E. Barbero. *Finite Element Analysis of Composite Materials using Abaqus.* CRC Press, 1 edition, 2013.

[7] S. Bargmann, B. Klusemann, J. Markmann, J. E. Schnabel, K. Schneider, C. Soyarslan, and J. Wilmers. Generation of 3d representative volume elements for heterogeneous materials: A review. *Progress in Materials Science*, 96:322–384, 2018.

[8] A. S. Bhatnagar, A. Gupta, G. Arora, S. Padmanabhan, and R. G. Burela. Mean-field homogenization coupled low-velocity impact analysis of nano fibre reinforced composites. *Materials Today Communications*, 26:102089, 2021.

[9] N. Biswas, J. Ding, V. Balla, D. Field, and A. Bandyopadhyay. Deformation and fracture behavior of laser processed dense and porous ti6al4v alloy under static and dynamic loading. *Materials Science and Engineering: A*, 549:213–221, 2012.

[10] F. Bobbert, K. Lietaert, A. Eftekhari, B. Pouran, S. Ahmadi, H. Weinans, and A. Zadpoor. Additively manufactured metallic porous biomaterials based on minimal surfaces: A unique combination of topological, mechanical, and mass transport properties. *Acta Biomaterialia*, 53:572–584, 2017.

[11] J. L. Calvo-Gallego, J. Martínez-Reina, and J. Domínguez. A polynomial hyperelastic model for the mixture of fat and glandular tissue in female breast. *International Journal for Numerical Methods in Biomedical Engineering*, 31(9):e02723, 2015.

[12] T. A. Carniel, B. Klahr, and E. A. Fancello. On multiscale boundary conditions in the computational homogenization of an rve of tendon fascicles. *Journal of the Mechanical Behavior of Biomedical Materials*, 91:131–138, 2019.

[13] R. Chandrasekaran, M. Hillgärtner, K. Ganesan, B. Milow, M. Itskov, and A. Rege. Computational design of biopolymer aerogels and predictive modelling of their nanostructure and mechanical behaviour. *Scientific Reports*, 11:10198, 2021.

[14] N. Charalambakis. Homogenization Techniques and Micromechanics. A Survey and Perspectives. *Applied Mechanics Reviews*, 63(3), 07 2010.

[15] G.-D. Cheng, Y.-W. Cai, and L. Xu. Novel implementation of homogenization method to predict effective properties of periodic materials. *Acta Mechanica Sinica*, 29:550–556, 2013.

[16] M. Colatosti, N. Fantuzzi, P. Trovalusci, and R. Masiani. New insights on homogenization for hexagonal-shaped composites as Cosserat continua. *MECCANICA*, 2021.

[17] L. Collini and A. Pirondi. Microstructure-based rve modeling of the failure behavior and lcf resistance of ductile cast iron. *Procedia Structural Integrity*, 24:324–336, 2019. AIAS 2019 International Conference on Stress Analysis.

[18] COMSOL-Multiphysics. Comsol multiphysics documentation. *Materials Letters*.

[19] A. Cuadrado, A. Yanez, O. Martel, S. Deviaene, and D. Monopoli. Influence of load orientation and of types of loads on the mechanical properties of porous ti6al4v biomaterials. *Materials Design*, 135:309–318, 2017.

[20] Z. Dong and X. Zhao. Application of tpms structure in bone regeneration. *Engineered Regeneration*, 2:154–162, 2021.

[21] M. Dumas, P. Terriault, and V. Brailovski. Modelling and characterization of a porosity graded lattice structure for additively manufactured biomaterials. *Materials Design*, 121:383–392, 2017.

[22] H. Elsayed, N. Novak, M. Vesenjak, F. Zanini, S. Carmignato, and L. Biasetto. The effect of strut size on microstructure and compressive strength of porous ti6al4v lattices printed via direct ink writing. *Materials Science and Engineering: A*, 787:139484, 2020.

[23] M. Esposito, J.-M. Hirsch, U. Lekholm, and P. Thomsen. Biological factors contributing to failures of osseointegrated oral implants, (i). success criteria and epidemiology. *European Journal of Oral Sciences*, 106(1):527–551, 1998.

[24] H. Gao, X. Jin, J. Yang, D. Zhang, S. Zhang, F. Zhang, and H. Chen. Porous structure and compressive failure mechanism of additively manufactured cubic-lattice tantalum scaffolds. *Materials Today Advances*, 12:100183, 2021.

[25] M. Geers, V. Kouznetsova, and W. Brekelmans. Multi-scale computational homogenization: Trends and challenges. *Journal of Computational and Applied Mathematics*, 234(7):2175–2182, 2010. Fourth International Conference on Advanced COmputational Methods in ENgineering (ACOMEN 2008).

[26] A. L. Gurson. Continuum theory of ductile rupture by void nucleation and growth: Part i-yield criteria and flow rules for porous ductile media. *Journal of Engineering Materials and Technology-transactions of The Asme*, 99:2–15, 1977.

[27] K. B. Hazlehurst, C. J. Wang, and M. Stanford. An investigation into the flexural characteristics of functionally graded cobalt chrome femoral stems manufactured using selective laser melting. *Materials Design*, 60:177–183, 2014.

[28] B. Herath, S. Suresh, D. Downing, S. Cometta, R. Tino, N. J. Castro, M. Leary, B. Schmutz, M.-L. Wille, and D. W. Hutmacher. Mechanical and geometrical study of 3d printed voronoi scaffold design for large bone defects. *Materials Design*, 212:110224, 2021.

[29] R. Hill. Elastic properties of reinforced solids: Some theoretical principles. *Journal of the Mechanics and Physics of Solids*, 11(5):357–372, 1963.

[30] M. Itskov. *Tensor Algebra and Tensor Analysis for Engineers: With Applications to Continuum Mechanics.* Springer Nature Switzerland AG 2019, 5 edition, 2019.

[31] M. Kaur and K. Singh. Review on titanium and titanium based alloys as biomaterials for orthopaedic applications. *Materials Science and Engineering: C*, 102:844–862, 2019.

[32] M. Kazempour, M. Baniassadi, H. Shahsavari, Y. Remond, and M. Baghani. Homogenization of heterogeneous brain tissue under quasi-static loading: a visco-hyperelastic model of a 3D RVE. *BIOMECHANICS AND MODELING IN MECHANOBIOLOGY*, 18(4):969–981, AUG 2019.

[33] A. Khoei and S. Saeedmonir. Computational homogenization of fully coupled multiphase flow in deformable porous media. *Computer Methods in Applied Mechanics and Engineering*, 376:113660, 2021.

[34] N. Kilingar, K. Ehab Moustafa Kamel, B. Sonon, T. Massart, and L. Noels. Computational generation of open-foam representative volume elements with morphological control using distance fields. *European Journal of Mechanics - A/Solids*, 78:103847, 2019.

[35] M. Lesueur, T. Poulet, and M. Veveakis. Predicting the yield strength of a 3d printed porous material from its internal geometry. *Additive Manufacturing*, 44:102061, 2021.

[36] D. Li and Y. Yao. An approximate method to predict the mechanical properties of small volume fraction particle-reinforced composites with large deformation matrix. *Acta Mechanica*, 230:3307â3315, 2019.

[37] K. Linka, M. Hillgärtner, K. P. Abdolazizi, R. C. Aydin, M. Itskov, and C. J. Cyron. Constitutive artificial neural networks: A fast and general approach to predictive data-driven constitutive modeling by deep learning. *Journal of Computational Physics*, 429:110010, 2021.

[38] S. Ma, Q. Tang, X. Han, Q. Feng, J. Song, R. Setchi, Y. Liu, Y. Liu, A. Goulas, D. S. EngstrÃ¸m, Y. Y. Tse, and N. Zhen. Manufacturability, mechanical properties, mass-transport properties and biocompatibility of triply periodic minimal surface (tpms) porous scaffolds fabricated by selective laser melting. *Materials Design*, 195:109034, 2020.

[39] M. McGregor, S. Patel, S. McLachlin, and Mihaela Vlasea. Architectural bone parameters and the relationship to titanium lattice design for powder bed fusion additive manufacturing. *Additive Manufacturing*, 47:102273, 2021.

[40] H. Mehboob, F. Tarlochan, A. Mehboob, and S.-H. Chang. Finite element modelling and characterization of 3d cellular microstructures for the design of a cementless biomimetic porous hip stem. *Materials Design*, 149:101–112, 2018.

[41] W. ming Peng, Y. feng Liu, X. feng Jiang, X. tao Dong, J. Jun, D. Baur, J. jie Xu, H. Pan, and X. Xu. Bionic mechanical design and 3d printing of novel porous ti6al4v implants for biomedical applications. *Journal of Zhejiang University. Science. B*, 20(8):647–659, 2019.

[42] M. Montemurro, G. Bertolino, and T. Roiné. A general multi-scale topology optimisation method for lightweight lattice structures obtained through additive manufacturing technology. *Composite Structures*, 258:113360, 2021.

[43] S. Munoz, S. Castillo, and Y. Torres. Different models for simulation of mechanical behaviour of porous materials. *Journal of the Mechanical Behavior of Biomedical Materials*, 80:88–96, 2018.

[44] nTopology. ntopology: Next-generation engineering design software documentation. 2022.

[45] S. L. Omairey, P. D. Dunning, and S. Sriramula. Development of an abaqus plugin tool for periodic rve homogenisation. *Engineering with Computers*, 35(2):567–577, 2018.

[46] J. M. Ortolano González, J. A. Hernández Ortega, and X. Oliver Olivella. *A comparative study on homogenization strategies for multi-scale analysis of materials.* Centre Internacional de Mètodes Numèrics en Enginyeria (CIMNE), 2013.

[47] D. Raabe, B. Sander, M. FriÃ¡k, D. Ma, and J. Neugebauer. Theory-guided bottom-up design of $\hat{I}^2 - titaniumalloysasbiomaterialsbasedonfirstprinciplescalculations : Theoryandexperiments. ActaMaterialia, 55(13) : 4475 - -4487, 2007.$

[48] A. Rege, M. HillgÃ¤rtner, and M. Itskov. Mechanics of biopolymer aerogels based on microstructures generated from 2-d voronoi tessellations. *The Journal of Supercritical Fluids*, 151:24–29, 2019.

[49] S. Ruiz de Galarreta, J. R. Jeffers, and S. Ghouse. A validated finite element analysis procedure for porous structures. *Materials Design*, 189:108546, 2020.

[50] T. B. Sercombe, X. Xu, V. Challis, R. Green, S. Yue, Z. Zhang, and P. D. Lee. Failure modes in high strength and stiffness to weight scaffolds produced by selective laser melting. *Materials Design*, 67:501–508, 2015.

[51] H. Shen and C. Brinson. A numerical investigation of the effect of boundary conditions and representative volume element size for porous titanium. *Journal of Mechanics of Materials and Structures*, 1:1179â1204, 2006.

[52] S. Shima and M. Oyane. Plasticity theory for porous metals. *International Journal of Mechanical Sciences*, 18(6):285–291, 1976.

[53] SLM-Solutions. Slm. 2022.

[54] A. J. Smith, P. Dieppe, K. Vernon, M. Porter, and A. W. Blom. Failure rates of stemmed metal-on-metal hip replacements: analysis of data from the national joint registry of england and wales. *The Lancet*, 379(9822):1199–1204, 2012.

[55] M. Somireddy and A. Czekanski. Computational modeling of constitutive behaviour of 3d printed composite structures. *Journal of Materials Research and Technology*, 11:1710–1718, 2021.

[56] N. Soro, H. Attar, X. Wu, and M. S. Dargusch. Investigation of the structure and mechanical properties of additively manufactured ti-6al-4v biomedical scaffolds designed with a schwartz primitive unit-cell. *Materials Science and Engineering: A*, 745:195–202, 2019.

[57] N. Soro, L. Brassart, Y. Chen, M. Veidt, H. Attar, and M. S. Dargusch. Finite element analysis of porous commercially pure titanium for biomedical implant application. *Materials Science and Engineering: A*, 725:43–50, 2018.

[58] M. Stoffel, F. Bamer, and B. Markert. Artificial neural networks and intelligent finite elements in non-linear structural mechanics. *Thin-Walled Structures*, 131:102–106, 2018.

[59] M. Suard, G. Martin, P. Lhuissier, R. Dendievel, F. Vignat, J.-J. Blandin, and F. Villeneuve. Mechanical equivalent diameter of single struts for the stiffness prediction of lattice structures produced by electron beam melting. *Additive Manufacturing*, 8:124–131, 2015.

[60] P. Szymczyk, V. Hoppe, G. Ziolkowski, M. Smolnicki, and M. Madeja. The effect of geometry on mechanical properties of ti6al4v eli scaffolds manufactured using additive manufacturing technology. *Archives of Civil and Mechanical Engineering*, 20:11–20, 2020.

[61] B. Tang, Q. Wang, N. Guo, J. Liu, H. Ge, Z. Luo, and X. Li. Microstructure-based rve modeling of ductile failure induced by plastic strain localization in tailor-tempered 22mnb5 boron steel. *Engineering Fracture Mechanics*, 240:107351, 2020.

[62] W. Tian, X. Chao, M. Fu, and L. Qi. An advanced method for efficiently generating composite rves with specified particle orientation. *Composites Science and Technology*, 205:108647, 2021.

[63] A. Trauth, L. Kehrer, P. Pinter, K. Weidenmann, and T. Böhlke. On the effective elastic properties based on mean-field homogenization of sheet molding compound composites. *Composites Part C: Open Access*, 4:100089, 2021.

[64] V. Tvergaard and A. Needleman. Analysis of the cup-cone fracture in a round tensile bar. *Acta Metallurgica*, 32(1):157–169, 1984.

[65] A. Vance, K. Bari, and A. Arjunan. Compressive performance of an arbitrary stiffness matched anatomical ti64 implant manufactured using direct metal laser sintering. *Materials Design*, 160:1281–1294, 2018.

[66] S. Vardak, S. Shatooti, and S. Zangeneh. Manufacturing of porous titanium using friction stir welding. *Materials Letters*, 310:131430, 2022.

[67] G. Voronoi. Nouvelles applications des paramÃ¨tres continus Ã la thÃ©orie des formes quadratiques. *Journal fÃ¼r die reine und angewandte Mathematik*, pages 198–287, 1908.

[68] S. Wang, L. Liu, K. Li, L. Zhu, J. Chen, and Y. Hao. Pore functionally graded ti6al4v scaffolds for bone tissue engineering application. *Materials Design*, 168:107643, 2019.

[69] X. Wang, L. Zhang, B. Song, J. Zhang, J. Fan, Z. Zhang, Q. Han, and Y. Shi. Anisotropic mechanical and mass-transport performance of ti6al4v plate-lattice scaffolds prepared by laser powder bed fusion. *Acta Biomaterialia*, 148:374–388, 2022.

[70] Z. Xia, Y. Zhang, and F. Ellyin. A unified periodical boundary conditions for representative volume elements of composites and applications. *International Journal of Solids and Structures*, 40(8):1907–1921, 2003.

[71] R. Yamanoglu, A. Bahador, and K. Kondoh. Fabrication methods of porous titanium implants by powder metallurgy. *Transactions of the Indian Institute of Metals*, 74:2555–2567, 2021.

[72] C. Yan, L. Hao, A. Hussein, and P. Young. Tiâ6alâ4v triply periodic minimal surface structures for bone implants fabricated via selective laser melting. *Journal of the Mechanical Behavior of Biomedical Materials*, 51:61–73, 2015.

[73] A. Yanez, A. Cuadrado, O. Martel, H. Afonso, and D. Monopoli. Gyroid porous titanium structures: A versatile solution to be used as scaffolds in bone defect reconstruction. *Materials Design*, 140:21–29, 2018.

[74] X. Yang, Q. Yang, Y. Shi, L. Yang, S. Wu, C. Yan, and Y. Shi. Effect of volume fraction and unit cell size on manufacturability and compressive behaviors of ni-ti triply periodic minimal surface lattices. *Additive Manufacturing*, 54:102737, 2022.

[75] A. Zaoui. Continuum micromechanics: Survey. *Journal of Engineering Mechanics*, 128(8):808–816, 2002.

[76] B. Zhang, X. Pei, C. Zhou, Y. Fan, Q. Jiang, A. Ronca, U. D'Amora, Y. Chen, H. Li, Y. Sun, and X. Zhang. The biomimetic design and 3d printing of customized mechanical properties porous ti6al4v scaffold for load-bearing bone reconstruction. *Materials Design*, 152:30–39, 2018.

A. Statement of authorship

I declare that this work has been composed by myself, and describes my own work, unless otherwise acknowledged in the text.

All sentences or passages quoted in this paper from other people's work have been specifically acknowledged by clear cross-referencing to author, work and page(s). Any photos and illustrations which are not the work of the author have been used with the explicit permission of the originator and are specifically acknowledged.

This work has not been and will not be submitted for any other degree or the obtaining of ECTS points at the RWTH Aachen University or any other institution of higher education.

Aachen, 28$^{\text{th}}$ of November 2022

_____

Noel Jacob Ureña Sandí, Lic. B.Sc.